Point Spread Function Engineering for Fluorescence Microscopy

by

Ratsimandresy Holinirina Dina Miora

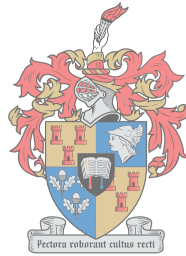

Thesis presented in partial fulfilment of the requirements for the degree of Master of Science (Physics) in the Faculty of Science at Stellenbosch University

Supervisors:

Dr. G. W. Bosman
Prof. E. G. Rohwer

March 2018

Stellenbosch University https://scholar.sun.ac.za

Declaration

By submitting this thesis electronically, I declare that the entirety of the work contained therein is my own, original work, that I am the sole author thereof (save to the extent explicitly otherwise stated), that reproduction and publication thereof by Stellenbosch University will not infringe any third party rights and that I have not previously in its entirety or in part submitted it for obtaining any qualification.

Date: March 2018

Copyright © 2018 Stellenbosch University
All rights reserved.

Stellenbosch University https://scholar.sun.ac.za

Abstract

Point Spread Function Engineering for Fluorescence Microscopy

R. Holinirina Dina Miora

Department of Physics,
Stellenbosch University,
Private Bag X1, Matieland 7602, South Africa.

Thesis: MSc

March 2018

A tool for biological imaging is developed within this work. It consists of engineering the point spread function (PSF) of a fluorescent molecule or a nanoparticle emitter by modulating the phase of the fluorescence emission. The engineered PSF developed in this current work is called the double helix point spread function (DH-PSF). Information about the three dimensional position of an emitter and its orientation can be extracted using this PSF with a very high precision and accuracy. Other modalities, such as the pyramidal PSF and the bisected PSF, are also simulated and compared theoretically with the efficiency of the DH-PSF.

Stellenbosch University https://scholar.sun.ac.za

Uittreksel

Puntverspreidingsfunksie Verstelling in Fluoressensie Mikroskopie

R. Holinirina Dina Miora

Fisika Departement,
Universiteit van Stellenbosch,
Privaatsak X1, Matieland 7602, Suid Afrika.

Tesis: MSc

Maart 2018

‘n Afbeeldingstegniek vir biologiese materie word in hierdie projek ontwikkel. Die tegniek behels die verstelling van die puntverspreidingsfunksie (PVF) van ‘n fluoresserende molekuul of nanopartikel deur die fase van die emissie te moduleer. In die huidige projek word daar gefokus op ‘n spesifieke PVF genaamd, dubbel helix puntverspreidingsfunksie (DH-PVF). Deur die korrekte toepassing van die DH-PVF is dit moontlik om hoë presisie en akkurate drie dimensionele posisie asook orientasie inligting van enkel fluoresserende voorwerpe te bepaal. Verder word daar ook ander modaliteite naamlik piramidale PVF en verdeelde PVF gesimuleer en met die DH-PVF vergelyk.

Stellenbosch University https://scholar.sun.ac.za

Acknowledgements

I would like to express my sincere gratitude to my supervisors, Prof Rohwer and Dr Bosman, for their patience and guidance, financial, and moral support throughout the entire research period. I am especially grateful for their sacrifice of time even during the holiday season. I would also like to thank Dr Bosman for accepting to write the Afrikaans version of the abstract of this thesis.

In addition, this work would not have been achieved without the financial and material support of the Stellenbosch University and the African Institute for Mathematical Sciences. My special thanks are extended to my friends, Charmaine for her help in the lab, Anneke, and Gina for their encouragement and their constructive advice during the writing of this thesis. Special thanks should be given to my parents, my family and friends, and my family here in Stellenbosch for their love, care, and prayers throughout my study.

Last but not least, I wish to acknowledge God for His input on this work. I challenged myself through this project for His glory.

Stellenbosch University https://scholar.sun.ac.za

Dedications

To my parents for their love and care,

Stellenbosch University https://scholar.sun.ac.za

Contents

Declaration i

Abstract ii

Uittreksel iii

Acknowledgements iv

Dedications v

Contents vi

List of Figures viii

List of Tables x

1 Introduction 1

2 Theory 2
- 2.1 Fluorescence microscopy . . . 2
- 2.2 Electromagnetic radiation . . . 5
- 2.3 Fourier imaging . . . 10

3 Experimental setup 29
- 3.1 Sample description . . . 29
- 3.2 Imaging system . . . 31
- 3.3 Axial positioning . . . 35

4 Localization analysis 39
- 4.1 Statistical models . . . 39
- 4.2 Localization limits . . . 40
- 4.3 Lateral localization precision and accuracy . . . 43
- 4.4 Experimental results for axial position using DH-PSF engineering 47
- 4.5 Simulated results of the orientation of a dipole emitter . . . 50

5 Conclusion 53

Stellenbosch University https://scholar.sun.ac.za

List of References **54**

Stellenbosch University https://scholar.sun.ac.za

List of Figures

2.1 Jablonski diagram indicating fluorescence, photobleaching and photoblinking electronic state transition 3
2.2 Dichroic beam splitter for separating the fluorescence emission from its excitation source 4
2.3 A dipole, oriented along the vector $\widehat{\eta}$, and its position vectors, $\widehat{r}_-$ and $\widehat{r}_+$, indicating the points where the electric field is to be evaluated 7
2.4 Thickness of a thin lens 12
2.5 Field propagation through a thin lens 13
2.6 Illustration of a convolution 15
2.7 Nematic liquid crystal microdisplay in a (a) parallel aligned structure and (b) twisted structure before and after an electric field is applied. 17
2.8 Schematic diagrams of electric and optical addressing mode for controlling an incident beam 18
2.9 A phase grating to improve the efficiency of an SLM 18
2.10 Point Spread Function in a 4f-type imaging system 19
2.11 Phase mask for generating a DH-PSF 21
2.12 Intensity pattern of a DH-PSF formed with a phase pattern composed by three rings with helical charges $1, 3$, and 5 22
2.13 Intensity pattern of an engineered PSF formed with a phase pattern composed by three rings with helical charges $5, 3$, and 1 respectively 23
2.14 Comparative images for different τ parameter 24
2.15 Image comparative of the double lobes intensity profile generated from a phase mask with helical charges $[1, 3, 5]$ and $[2, 4, 6]$. 24
2.16 Dipole orientation. 25
2.17 Schematic representation of the 4f imaging system employed to investigate the single dipole DH-PSF 26
2.18 Intensity pattern of the field from a dipole emitter with different orientations evaluated at the back focal plane 27
2.19 Simulated DH-PSF for a dipole oriented with $(\Theta, \Phi) = (45°, 90°)$ and emitting light with wavelength $\lambda = 550$ nm 28

3.1 Photobleaching decay of a 50 nm fluorescent silica nanobead 31
3.2 Schematic diagram of experimental setup 32

Stellenbosch University https://scholar.sun.ac.za

3.3 Use of the USAF 1951 test target for finding the imaging calibration factor . . . 34
3.4 Michelson interferometer for measuring optical pathlength difference between two mirrors . . . 36
3.5 Interference intensity profile as a function of the applied voltage on the piezoelectric . . . 38
3.6 Phase shifting parameter as a function of the applied voltage. . . . 38

4.1 Single nanoparticle emission . . . 43
4.2 Localization accuracy of nanoparticle emitters . . . 46
4.3 Image comparatives of the DH-PSF from experimental results and simulated DH-PSFs of an isotropic emitter with NA = 0.86 and NA = 1.3 for different defocus distances d . . . 48
4.4 The angle of the rotation line of the two lobes changes monotonically as a function of the z position . . . 49
4.5 Lobe asymmetry of the two lobes in horizontal channel and vertical channel, and linear dichroism at the focal plane with defocus distance 0. . . . 51
4.6 Phase masks for bisected and pyramidal PSFs . . . 52
4.7 Bisected and pyramidal PSF of an isotropic and a dipole emitter at different defocus distance d . . . 52

Stellenbosch University https://scholar.sun.ac.za

List of Tables

4.1 Results for lateral localization analysis 47

Stellenbosch University https://scholar.sun.ac.za

Chapter 1

Introduction

Over the past two decades, progress in super-resolution microscopic techniques allowed for biological investigations in living cells to nanometer length scales and milliseconds timescales [1]. This advancement in microscopy meant that apart from the structural and morphological characterization of cells, intracellular transport mechanism and interaction mapping are now readily investigated [2]. For that reason super-resolution microscopy is currently an essential tool for all research laboratories in the area of applied biophotonics.

Therefore, the aim of this work is to extend the capabilities of a wide-field fluorescence microscope to achieve simultaneous 3D localization, and to find the orientation of a single emitter with a high accuracy and precision by engineering the point spread function (PSF) of the emitter light source. A fluorescent nanoparticle, embedded in a polymer media, is used as emitter source. The technique consists of modulating the phase of the fluorescence emission of the emitter using a Fourier processing imaging technique.

The work is divided into three chapters. The first chapter introduces readers to a theoretical study of wide-field fluorescence microscopy, the propagation of light, and an introduction to Fourier imaging. A modelisation of the dipole emission and the phase modulation of the radiation into a double helix point spread function (DH-PSF) in order to retrieve the axial position of the dipole is also developed in the first chapter. The second chapter describes the experimental apparatus for experimental validation of the theory developed in chapter one. A 4f-type imaging system is used for such kind of experiment and is coupled with a piezoelectric stage to control the axial position. The sample preparation and description and calibration are given in details in this chapter. The third chapter highlights the localization results of single emitters using a DH-PSF engineering technique. A theoretical study of the Fischer information matrix is developed to determine the limit of the localization precision. The lateral and axial position for typical emitters are investigated. Other PSFs: bisected PSF and pyramidal PSF are illustrated as a path towards improved optical resolution in fluorescence microscopy.

Stellenbosch University https://scholar.sun.ac.za

Chapter 2

Theory

Engineering the emission pattern of a single emitter requires sufficient understanding of the generation of light, the propagation of light and the relevant mathematical models to describe the aforementioned. This section gives a theoretical background of a wide-field fluorescence microscopy, electromagnetic radiation, and an introduction to Fourier imaging.

2.1 Fluorescence microscopy

Fluorescence microscopy is a technique which uses fluorescence properties of molecules in order to achieve high resolution optical imaging. Fluorescent molecules are often used in imaging as probes or as dyeing objects for biological molecules. There are many types of fluorescent objects such as organic dyes, semiconductor nanoparticles, nanoparticles with size-dependent optical and physicochemical properties, gold nanoparticles and green fluorescent proteins [3]. The terms of use of a specific fluorescent molecule depends on its optical and physicochemical properties. Physicochemical properties regroup the size and the ability of the molecule to react with its environment, while optical properties refer to the interaction of the molecule with an electromagnetic radiation field such as a laser source. Optical properties consist of the excitation spectrum, extinction coefficient, emission spectrum, fluorescence quantum yield (QY), molecular brightness and photostability of the molecule [4].

In a large number of applications it is required for a fluorescent object to be photostable. However in practice it is readily observed that the fluorescence intensity typically shows a steady decline (photobleaching) with time or in the case of single fluorescent molecules also a rapid on and off (photoblinking) switching. In order to understand the photo-physical origin of the effects consider the Jablonski diagram in Figure 2.1. Fluorescence, photobleaching, and photoblinking are described by the transition between three level states: singlet state S, triplet state T, and an anion state D. Fluorescence is observed

Stellenbosch University https://scholar.sun.ac.za

between two singlet states. A fluorescent molecule is excited from its ground state S_0 to an excited state S_1 when it absorbs light from an external source, usually called an excitation source. An excited state is an unstable state, thus the molecule emits fluorescent light in order to reach the stable ground state S_0 [5]. Furthermore, it must be noted that the number of emitted photons in a fluorescence process is characterized by the quantum yield and the extinction coefficients of the fluorescent emitter, and the excitation source.

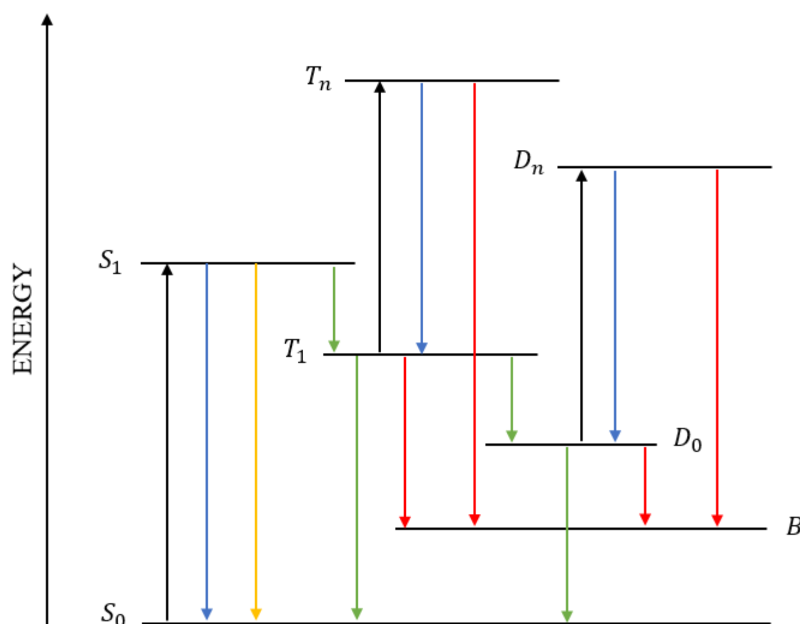

Figure 2.1: *Jablonski diagram indicating fluorescence, photobleaching and photo-blinking electronic state transition. S, T, D, and B denote singlet, triplet, anion, and bleaching state respectively.* ***Black*** *arrows indicate the absorption of energy yielding a higher energy level. The* ***orange*** *arrow corresponds to the fluorescence emission between two singlet states.* ***Blue*** *arrows indicate non-radiative internal conversion.* ***Green*** *arrows indicate non-radiative intersystem crossing, transitions between states with different spin multiplicity. A radiative intersystem crossing is a phosphorescence process.* ***Red*** *arrows show the transitions yielding the bleaching state. Photoblinking process happens when there is a non-stationary reversible transitions between states.*

Photobleaching and photoblinking happen once a triplet and/or anion state are involved [6]. Photobleaching is an irreversible process where the emitter's ability to fluoresce decreases with time. The photobleaching rate depends on the intensity of the excitation source and its reaction or interaction with its environment [5]. An emitter embedded in two different medias therefore does not bleach or blink at the same rate. The state B in Figure 2.1 corresponds to the bleaching state. A bleaching state is a state where the molecule cannot fluoresce anymore. On the other hand, photoblinking is an on/off random switch process characterized as non-stationary reversible transitions between

Stellenbosch University https://scholar.sun.ac.za

states. Thus, when the molecule blinks, it fluoresces, then does not fluoresce, and so on.

Forming an image of fluorescent objects requires the effective separation of the fluorescence and the excitation source. The fluorescence has a lower photon energy than the excitation light, and therefore propagates with a longer wavelength. Accordingly, there is an energy difference between the emitted and excitation light. This energy difference is commonly referred to as the Stokes shift and is a very important parameter to consider when designing a microscope.

The separation of the excitation light and emitted light is achieved using a dichroic beam splitter and filters (Figure 2.2). A dichroic beam splitter and filters work based on the optical thin film interference principle. A dichroic beam splitter selectively reflects light within a certain range of wavelengths and transmit light out of that wavelength range while a filter blocks the light within an unwanted wavelength range.

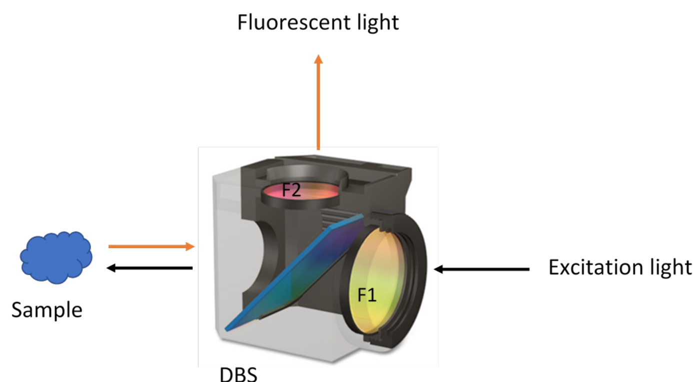

Figure 2.2: *Dichroic beam splitter. The excitation source is incident on the excitation filter $F1$ and passes through the dichroic beam splitter (DBS) to excite the sample. When the sample is excited, it emits fluorescent light. The fluorescent light is reflected by the DBS, while the excitation light is transmitted. The second filter $F2$ serves as an emission filter.*

The localization precision and accuracy of each single fluorescent object is very important in fluorescence microscopy. The localization precision is proportional to the standard deviation of the estimated molecule's position around the average position, and inversely proportional to the square root of the number of photons collected from an emitter. Whilst the localization accuracy is defined as the distance between the average position and the true position. When a fluorescent object bleaches, the number of emitted photons decreases with time so imaging the emitter becomes difficult and is not accurate. A bright emitter allows a precise and accurate localization.

Stellenbosch University https://scholar.sun.ac.za

There are quite a number of basic microscopy techniques for imaging fluorescence radiation such as confocal microscopy, two-photon microscopy and wide-field microscopy [7]. In this project, a wide-field fluorescence microscope is used, because of its ability to excite and image uniformly over a large area of sample without the need for scanning, and as such, results in high detection speeds [7].

A basic understanding of electromagnetic radiation is required in order to gain insight into the behaviour and nature of the fluorescent emission of objects. In the next section, this is addressed by introducing the theoretical foundations of electromagnetic radiation as well as an overview of Fourier imaging.

2.2 Electromagnetic radiation

The theory of electromagnetic radiation is introduced in the first part of this section. This is then followed by the derivation of the electromagnetic field of a dipole radiator. The radiation from a dipole radiator is considered as an approximation to the single molecule fluorescent emission.

2.2.1 Electromagnetic theory

The electromagnetic theory has its origin in Coulomb's law, first stated by a French physicist named Charles Augustin de Coulomb around 1985 [8]. The law describes the fundamental interaction of electric charges through the electrostatic force. At rest, a point charge q_i exerts a force $\overrightarrow{F_i}$ on a charge Q with magnitude

$$|\overrightarrow{F_i}(r_i)| = \frac{1}{4\pi\epsilon_0}\frac{q_i Q}{r_i^2}, \quad i \in \mathbb{N} \tag{2.2.1}$$

where r_i is the distance between q_i and Q, and ϵ_0 is the permittivity of free space.

The electrostatic force experienced by the two charged objects is mediated through the inherent electric field of each object. This connection between force and field for a point charge is summed up in the definition of the electric field for a charge Q as the force per unit charge [9].

$$\overrightarrow{E}(r) = \frac{\overrightarrow{F}(r)}{Q}, \tag{2.2.2}$$

where r is the magnitude of the position vector $\overrightarrow{r}$.

The Lorentz force law followed Coulomb's law. It states that when a charge is in motion, it will also experience a magnetic force due to a magnetic field $\overrightarrow{B}$ [9]. The magnetic force on a charge q_i moving with vector velocity $\overrightarrow{v}$ is defined as

$$\overrightarrow{F}_{\text{mag}}(r_i, t) = q_i(\overrightarrow{v} \times \overrightarrow{B}(r_i, t)), \tag{2.2.3}$$

Stellenbosch University https://scholar.sun.ac.za

where $\overrightarrow{B}$ is the magnetic-flux density.

In the presence of both the electric field and the magnetic field, the total force on the charge Q is given by

$$\overrightarrow{F}(r,t) = Q[\overrightarrow{E}(r,t) + (\overrightarrow{v} \times \overrightarrow{B}(r,t))]. \tag{2.2.4}$$

In around 1820, Ampere, Biot and Savart discovered experimentally a relation between the magnetic fields and the electric currents. Those experiments pointed towards the interdependence between the magnetic and electric fields [9].

Following the work of many physicists in the nineteenth century on the electric and magnetic fields, Maxwell established four equations describing the combination of an electric field and magnetic field in 1873: the electromagnetic field [10]. The four equations are given as follows:

$$\nabla \cdot \overrightarrow{E}(r,t) = \frac{\rho}{\epsilon_0} \tag{2.2.5}$$

$$\nabla \cdot \overrightarrow{B}(r,t) = 0 \tag{2.2.6}$$

$$\nabla \times \overrightarrow{E}(r,t) = -\frac{\partial \overrightarrow{B}(r,t)}{\partial t} \tag{2.2.7}$$

$$\nabla \times \overrightarrow{B}(r,t) = \mu_0 \overrightarrow{J}(r,t) + \epsilon_0 \mu_0 \frac{\partial \overrightarrow{E}(r,t)}{\partial t} \tag{2.2.8}$$

where ρ is the source charge density, μ_0 is the vacuum permeability, and $\overrightarrow{J}$ is the current per unit area.

Equations (2.2.5) and (2.2.6) are Gauss's law for electricity and magnetism respectively, which underpin the source of electric fields, and also illustrate the nature of magnetic fields [10]. Equation (2.2.7) is Faraday's law of induction. As the negative rate of the magnetic field through the electric field lines changes, the circulation of the electric field changes as well. Thus, a time-varying magnetic field generates an electric field [11]. The last Maxwell's equation generalizes Ampere's law. The second term on the right hand side of Equation (2.2.8) states that a time-varying electric field also generates a magnetic field. Also, in the presence of an electric current per unit cross-section area $\overrightarrow{J}$, there is always a magnetic field. If the rate of change of the electric field is constant, then the magnetic field remains invariant [8]. In free space, $\overrightarrow{J}$ and ρ are zero which leads to a symmetry in Maxwell's equations and an interdependence between the electric and magnetic field. Solving the four Maxwell's equations leads to the wave equation which illustrates the wave nature of electromagnetic radiation.

Stellenbosch University https://scholar.sun.ac.za

2.2.2 Electric field of a Dipole

Electromagnetic radiation within the visible spectrum is commonly referred to as light and can be described as waves propagating through space carrying energy. A dye molecule emits light (fluorescence) when it is excited from its ground state to another state. In this work, it is assumed that the fluorescence of a single dye molecule can be approximated as being akin to that of dipole radiation. A typical electric dipole is characterized by its moment which measures the separation between the "positive" and "negative" ends of a system [8].

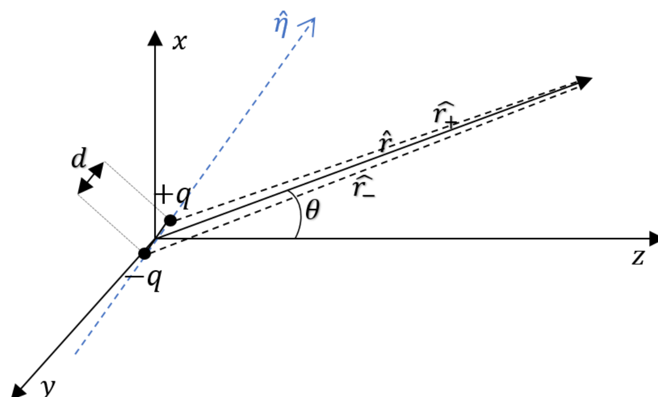

Figure 2.3: *A dipole, oriented along the vector $\widehat{\eta}$, and its position vectors, $\widehat{r}_-$ and $\widehat{r}_+$, indicating the points where the electric field is to be evaluated. The position vector $\widehat{r}$ is the vector sum of the two position vectors, $\widehat{r}_-$ and $\widehat{r}_+$.*

Dipole moment

A dipole consists of two charged particles with same magnitude charge, but opposite sign ($+q$ and $-q$), and separated by a distance d (or displacement vector $\overrightarrow{d} = d\widehat{\eta}$). A dipole moment $\overrightarrow{p}$ is a vector quantity equal to $qd\widehat{\eta}$ (Figure 2.3). This quantity reveals the orientation of the dipole in space. In polar coordinates, the orientation is read as

$$\widehat{\eta} = \begin{pmatrix} \sin\Theta\cos\Phi \\ \sin\Theta\sin\Phi \\ \cos\Theta \end{pmatrix}, \tag{2.2.9}$$

where Θ is the polar angle, and Φ the azimuthal angle.

Static dipole

Firstly, let us consider a static dipole with a dipole moment $\overrightarrow{p}$. Here static implies that the dipole moment is assumed to be independent of time. We

Stellenbosch University https://scholar.sun.ac.za

shall evaluate the electric field of a static dipole at a given position r along the vector $\widehat{r}$ defined by

$$\widehat{r} = \begin{pmatrix} \sin\theta\cos\phi \\ \sin\theta\sin\phi \\ \cos\theta \end{pmatrix}, \tag{2.2.10}$$

where θ and ϕ are the polar and the azimuthal angles respectively. The electric field from a static dipole evaluated at a given position with magnitude r is:

$$\overrightarrow{E}(r) = \frac{1}{4\pi\epsilon_0}\left(\frac{3(\overrightarrow{p}\cdot\widehat{r})\widehat{r} - \overrightarrow{p}}{r^3}\right) - \frac{1}{3\epsilon_0}\overrightarrow{p}\delta^3(r), \tag{2.2.11}$$

where δ^3 is the three dimensional delta function [12].

Oscillating dipole

For a time dependent dipole, we consider the case where the dipole is harmonically oscillating in time with an angular frequency ω. The dipole moment, which remains along the $\widehat{\eta}$ vector with a magnitude of p_0, is then defined as

$$\overrightarrow{p}(t) = p_0 e^{-iwt}\widehat{\eta}. \tag{2.2.12}$$

The electric field produced by this oscillating dipole [12] is given by

$$\overrightarrow{E}(r,t) = \frac{1}{4\pi\epsilon_0}\left(\frac{w^2}{c^2 r}(\widehat{r}\times\overrightarrow{p})\times\widehat{r} + \left(\frac{1}{r^3} - \frac{iw}{cr^2}\right)\left[3\widehat{r}(\widehat{r}\cdot\overrightarrow{p}) - \overrightarrow{p}\right]\right) e^{\frac{iwr}{c}} e^{-iwt}. \tag{2.2.13}$$

The magnetic field on the other hand is obtained from the retarded potential formulation as

$$\overrightarrow{B}(r,t) = \frac{w^2}{4\pi\epsilon_0 c^3}\widehat{r}\times\overrightarrow{p}\left(1 - \frac{c}{i\omega r}\right)\frac{e^{\frac{i\omega r}{c}}}{r}e^{-i\omega t}. \tag{2.2.14}$$

Further simplifications of the magnetic and electric field at large distance from the source, in the so-called "radiation zone" where $r \gg \frac{c}{w}$ yield

$$\overrightarrow{B}(r,t) = \frac{w^2}{4\pi\epsilon_0 c^3}\widehat{r}\times\overrightarrow{p}\frac{e^{\frac{i\omega r}{c}}}{r}e^{-i\omega t} \tag{2.2.15}$$

and

$$\overrightarrow{E}(r,t) = c\overrightarrow{B}\times\widehat{r}. \tag{2.2.16}$$

Equation (2.2.15) and (2.2.16) are theoretical expressions of the electric and magnetic field of a dipole. In much the same way, the electric field generated by a dipole can also be derived using Green's function which results in a treatment which is trivial to implement in computer simulations. For this reason a short summary of the derivation for the electric field of a dipole is shown.

Stellenbosch University https://scholar.sun.ac.za

2.2.3 Derivation of the electric field using Green's function

Green's function is a valuable tool for solving non-homogeneous linear equations. Let us assume that the electric field is proportional to the Green's function such that

$$\overrightarrow{E}(r) = w^2 \mu_0 \mu \overline{G}(r) \overrightarrow{\eta}, \tag{2.2.17}$$

where $\overline{G}$ is the dyadic Green's function, and μ_0 is the vacuum permeability [10].

A linear inhomogeneous equation for the Green's function is of the form

$$\mathcal{L}\overrightarrow{G_i}(r) = \widehat{n_i}\delta(r), \tag{2.2.18}$$

where $\mathcal{L}$ is a linear operator, $\overrightarrow{G_i}$ is the Green's function along the $i-$axis directed by the unit vector $\widehat{n_i}$ and δ is the Dirac delta function, which is zero except at $r = 0$. In terms of the unit dyadic $\overline{I}$, the Equation (2.2.18) can be written as

$$\mathcal{L}\overline{G}(r) = \overline{I}\delta(r). \tag{2.2.19}$$

The unit dyadic is the unit tensor represented by a 3×3 identity matrix. A dyadic product is a tensor.

The linear operator $\mathcal{L}$ is the Helmholtz operator. The inhomogeneous Helmholtz equation allows a derivation of the scalar Green's function G_0

$$[\nabla^2 + k^2]G_0(r) = -\delta(r), \tag{2.2.20}$$

where k is the wave number. Solving Equation (2.2.20) for an homogeneous space yields to the only physical solution in free space [10]

$$G_0(r) = \frac{e^{\pm ikr}}{4\pi r}. \tag{2.2.21}$$

Thus,

$$\overline{G}(r) = \left[\overline{I} + \frac{1}{k^2}\nabla\nabla\right] G_0(r). \tag{2.2.22}$$

In cartesian coordinates, the dyadic Green's function can be written as

$$\overline{G}(r) = \left[\left(1 + \frac{ikr - 1}{k^2r^2}\right)\overline{I} + \frac{3 - 3ikr - k^2r^2}{k^2r^2}\frac{rr^\dagger}{r^2}\right] G_0(r), \tag{2.2.23}$$

$\dagger$ is the adjoint operator.

Stellenbosch University https://scholar.sun.ac.za

This expression can be splitted into three [10]:

$$\overline{G}(r) = \left(\overline{I} - \frac{rr\dagger}{r^2}\right) G_0(r) + \frac{i}{kr}\left(\overline{I} - 3\frac{rr\dagger}{r^2}\right) G_0(r) + \frac{i}{k^2r^2}\left(-\overline{I} + 3\frac{rr\dagger}{r^2}\right) G_0(r). \tag{2.2.24}$$

The dyadic Green's function is a 3×3 matrix. The first term, the second term and the third term of Equation (2.2.24) are respectively proportional to r^{-1}, r^{-2}, and r^{-3}. In the far field where $r \gg \lambda$, only the first term remains. The second and the last term correspond to the intermediate field where $r \approx \lambda$ and the near field where $r \ll \lambda$ respectively.

In a non-dispersive medium with refractive index n, the scalar Green's function G_0 can be substituted by $\frac{e^{inkr}}{4\pi r}$ [10].

Therefore, the electric field of a radiating dipole in a non-dispersive medium with refractive index n can be approximated in terms of the Green's function as follows

$$\overrightarrow{E}(r) = w^2\mu_0\mu\frac{e^{inkr}}{4\pi r}\left(\overline{I} - \frac{rr^\dagger}{r^2}\right)\overrightarrow{\eta}. \tag{2.2.25}$$

In the following section, a Fourier imaging technique for modulating the phase or amplitude or polarization of an electric field is developed.

2.3 Fourier imaging

Imaging of an object is seen as a one-to-one mapping from an object space to an image space. This mapping can be described mathematically through appropriate Fourier formulations [13]. In this project, we focus on a particular case of Fourier analysis for the propagation of light through optical elements (like lenses).

A Fourier transform $\mathcal{F}$ of a function g of three independent variables x, y, z is the complex-valued function G defined by

$$\begin{aligned} G(f_x, f_y, f_z) &= \mathcal{F}[g(x,y,z)] \\ &= \iiint_{-\infty}^{\infty} g(x,y,z)\exp[-2\pi i(f_x x + f_y y + f_z z)]\, dx\, dy\, dz, \end{aligned} \tag{2.3.1}$$

where f_x, f_y, f_z are the frequencies for each channel x, y, z respectively.

Stellenbosch University https://scholar.sun.ac.za

The inverse Fourier transform $\mathcal{F}^{-1}$ of the function G is

$$\begin{aligned} g(x,y,z) &= \mathcal{F}^{-1}[G(f_x,f_y,f_z)] \\ &= \iiint_{-\infty}^{\infty} G(f_x,f_y,f_z)\exp[2\pi i(f_x x + f_y y + f_z z)]\, df_x\, df_y\, df_z. \end{aligned} \quad (2.3.2)$$

The Fourier transform of the function g exists if the following conditions are satisfied [14]

- g is absolutely integrable over the infinite space,
- g has only a finite number of discontinuities and a finite number of minima and maxima in any finite subspace,
- g has no infinite discontinuities.

Electromagnetic fields generally satisfies these three conditions. In the next section, the Fourier property of a thin lens and its use to form an image of a field source are demonstrated.

2.3.1 Optical image formation with a thin lens

A lens is the most useful optical element in optical imaging. Lenses are mostly made of glass, which is characterised by a given refractive index. In this section, let consider a lens with refractive index n and whose radius of curvature of the left-hand and right-hand surface are R_1 and R_2 respectively (Figure 2.4). Let us assume that the incident rays on one surface of the lens and the emergent rays on the opposite surface are approximately at the same point (x, y). Within such an assumption, the lens is assumed to be thin [13]. The phase delay, $\phi(x, y)$ at (x, y), caused by the lens depends on the thickness, $\Delta(x, y)$, of the lens at that position.

Transfer function of a thin lens

A lens is characterized by its thickness function. The thickness is maximum and equal to Δ_0 at the lens axis. Goodman demonstrates in detail in his book [13], that the expression of the thickness function can be generated by splitting the lens into two parts within the paraxial approximation. The thickness function of a thin lens is given by

$$\Delta(x,y) = \Delta_0 - \frac{x^2+y^2}{2}\left(\frac{1}{R_1} - \frac{1}{R_2}\right). \quad (2.3.3)$$

Since the surface of the lens is not planar, the phase delay $\phi(x, y)$ caused by the lens is set to be equal to the sum of the phases due to the free space between the transverse plane at the center of lens and the transverse plane at (x, y), and the phase due to the lens itself. The free space is usually air with

Stellenbosch University https://scholar.sun.ac.za

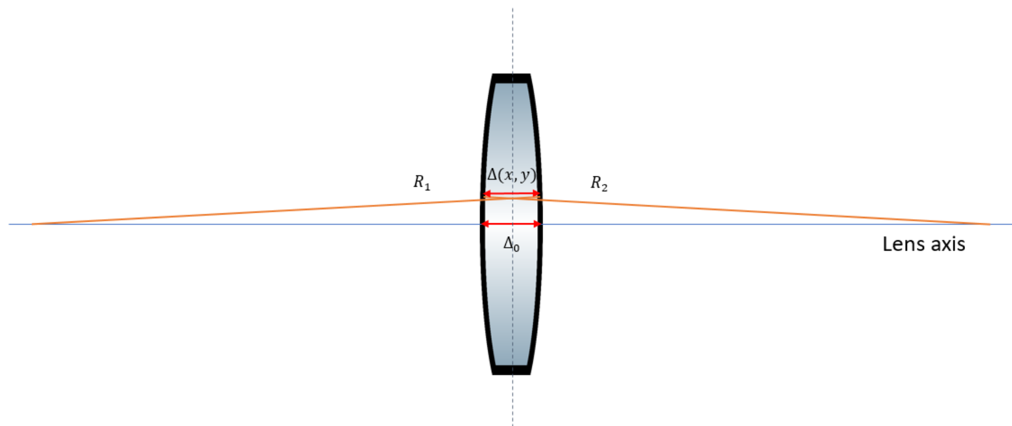

Figure 2.4: *Thin lens. It has two surfaces with respective radius of curvatures R_1 and R_2. The thickness $\Delta(x, y)$ of the lens is maximum at the lens axis and equal to Δ_0 at that position.*

refractive index equal to 1. Taking this into consideration leads to a phase delay of

$$\begin{aligned} \phi(x, y) &= k[\Delta_0 - \Delta(x, y)] + kn\Delta(x, y) \\ &= k[\Delta_0 + (n - 1)\Delta(x, y)] \end{aligned} \tag{2.3.4}$$

Hence the transfer function[1] of the lens is given by

$$t_l(x, y) = e^{ik\Delta_0} e^{ik(n-1)\Delta(x,y)} \tag{2.3.5}$$

Here, k is the magnitude of the vacuum wave vector (propagation vector). The transfer function of the lens illustrates that the lens acts as an optical device which ideally only alters the phase of light. In the next section, it is demonstrated, that together with the derived transfer function (2.3.5), a lens can act a Fourier transform operator.

Fourier property of a lens

In order to understand the Fourier property of a lens, the propagation of an electric field from a point source object to an imaging plane, passing through a thin lens is explained step by step. Let $U_0 = At_0$ be the transmitted field of light from an object placed at distance d_0 in front of the lens where A is the amplitude and t_0 the transmittance of the object. The field U_0 is incident on the lens and propagates like an electromagnetic field in space (Figure 2.5). The phase and amplitude of the incident field may change along the way as it propagates depending on the medium in which it travels.

[1] A transfer function is a mathematical formulation representing a material, such as lens, whose operation gives a corresponding output for each input on the material.

Stellenbosch University https://scholar.sun.ac.za

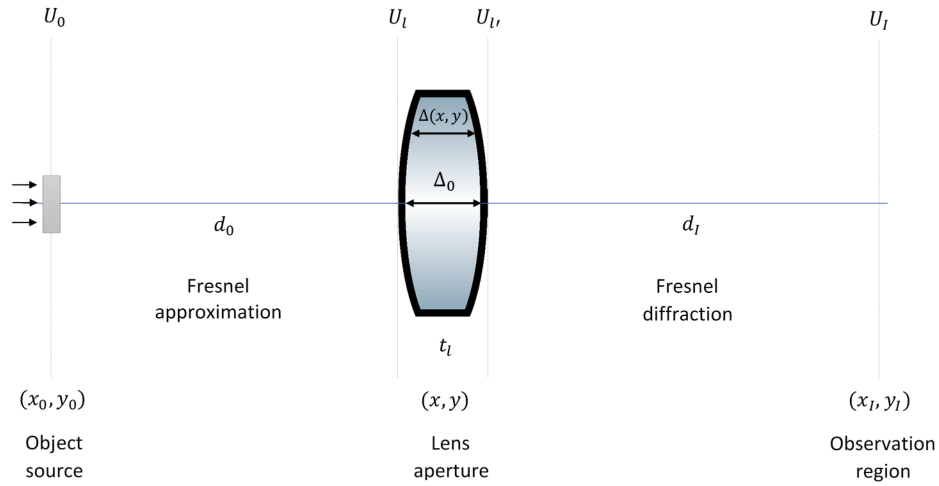

Figure 2.5: *Field propagation through a thin lens. U_0 : transmitted field from an object placed at distance d_0 in front of a thin lens, U_l : field in front of the lens, $U_{l'}$: field just after passing through the lens, and U_I : field at the image plane.*

During the propagation over the distance d_0, the light is subject to the Fresnel approximation where d_0 is sufficiently large and much greater than the finite region, defined as the region of interest, illuminated by the field on the lens. The transfer function for this region is given in spatial frequency domain [13] by

$$H(d_x, d_y) = e^{ikd_0} e^{-ik\lambda d_0 (d_x^2 + d_y^2)}, \tag{2.3.6}$$

where $d_x = \frac{x}{\lambda d_0}$ and $d_y = \frac{y}{\lambda d_0}$ are the spatial frequencies along the x and y direction respectively, and (x, y) constitute the coordinates system on the lens.

The Fourier spectrum of the transmitted field U_0 is defined as

$$\begin{aligned} F_0(d_x, d_y) &= \mathcal{F}[At_0] \\ &= A \iint_{-\infty}^{+\infty} t_0(x_0, y_0) e^{-i2\pi(x_0 d_x + y_0 d_y)}\, dx_0\, dy_0. \end{aligned} \tag{2.3.7}$$

The Fourier spectrum of the incident field on the lens is then obtained by

$$F_l(d_x, d_y) = H(d_x, d_y) F_0(d_x, d_y). \tag{2.3.8}$$

Also,

$$F_l(d_x, d_y) = \mathcal{F}[U_l]. \tag{2.3.9}$$

Stellenbosch University https://scholar.sun.ac.za

On the other hand, the field just after passing through the lens is given by

$$U_{l'}(x,y) = t_l(x,y)U_l(x,y), \tag{2.3.10}$$

where t_l is the transfer function of the lens defined in Equation (2.3.5).

Over the region between the lens and the observation region or image plane illustrated in Figure 2.5, the field $U_{l'}$ is influenced by the law of the Fresnel diffraction [13]. Hence, the field at distance d_I behind the lens is given by

$$U_I(x_I,y_I) = \frac{e^{ikd_I}}{i\lambda d_I} e^{\frac{ik}{2d_I}(x_I^2+y_I^2)} \iint_{-\infty}^{+\infty} U_{l'}(x,y) e^{\frac{ik}{2d_I}(x^2+y^2)}\, e^{-\frac{i2\pi}{\lambda d_I}(xx_I+yy_I)}\, dx\, dy, \tag{2.3.11}$$

(x_I, y_I) are coordinates in the image plane.

Using the Equation (2.3.10), and evaluating the field at distance $d_I = f$, where f is the focal length of the lens, Equation (2.3.11) becomes

$$U_f(x_f,y_f) = \frac{e^{ikf}}{i\lambda f} e^{\frac{ik}{2f}(x_f^2+y_f^2)} \iint_{-\infty}^{+\infty} U_l(x,y) e^{-\frac{i2\pi}{\lambda f}(xx_f+yy_f)}\, dx\, dy. \tag{2.3.12}$$

From this expression, we notice that

$$\iint_{-\infty}^{+\infty} U_l(x,y) e^{-\frac{i2\pi}{\lambda f}(xx_f+yy_f)}\, dx\, dy = \mathcal{F}[U_l] \tag{2.3.13}$$

which is the Fourier spectrum of U_l.
Equation (2.3.8), (2.3.9), and (2.3.12) give us the equality

$$U_f(x_f,y_f) = \frac{e^{ikf}}{i\lambda f}\, e^{\frac{ik}{2f}(x_f^2+y_f^2)} H(d_x,d_y)\mathcal{F}[At_0]. \tag{2.3.14}$$

Using the paraxial approximation, it can be shown that $(x_f^2 + y_f^2) \approx (x^2 + y^2)$ for $k = \frac{2\pi}{\lambda}$. Thus, the field at the back focal plane of the lens is

$$U_f(x_f,y_f) = A\frac{e^{ik(f+d_0)}}{i\lambda f}\, e^{\frac{ik}{2f}(x_f^2+y_f^2)(1-\frac{f}{d_0})} \iint_{-\infty}^{+\infty} t_0(x_0,y_0) e^{-i2\pi(x_0 d_x + y_0 d_y)}\, dx_0\, dy_0. \tag{2.3.15}$$

If the object is placed at distance $d_0 = f$ in front of the lens, the field at the image plane is exactly the Fourier transform of the transmitted field U_0 within a factor $\frac{e^{2ikf}}{i\lambda f}$

$$U_f(x_f,y_f) = A\frac{e^{2ikf}}{i\lambda f} \iint_{-\infty}^{+\infty} t_0(x_0,y_0) e^{-i2\pi(x_0 f_x + y_0 f_y)} dx_0 dy_0 \tag{2.3.16}$$

with spatial frequencies $f_x = \frac{x_f}{\lambda f}$ and $f_y = \frac{x_y}{\lambda f}$.

Hence, a lens has a particular Fourier property, which is very useful in optical imaging. The next section generalizes the inherent phase modulation capabilities within Fourier imaging.

Stellenbosch University https://scholar.sun.ac.za

2.3.2 Phase modulation

Convolution theorem

The convolution theorem describes a modulation process. Let us define two functions $u = u_0 e^{i\phi}$ and $v = v_0 e^{i\varphi}$ whose Fourier transforms exist under the three conditions stated in Section 2.3 [14]. A convolution is, by definition, the operation on two given functions u and v deriving a new function such that the shape of this new function is basically the shape of u (v respectively), but modified by v (u respectively) (Figure 2.6).

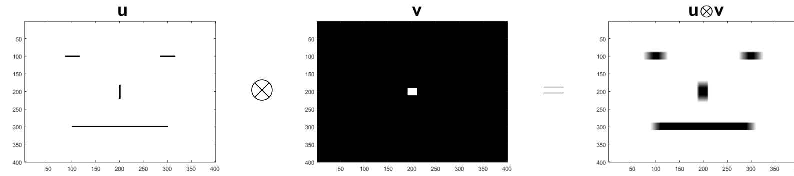

Figure 2.6: *Illustration of a convolution. The image illustrated as v object is like a paint brush for u, giving $u \otimes v$.*

The convolution theorem is stated mathematically as follows

$$\mathcal{F}[u \otimes v] = \mathcal{F}[u]\mathcal{F}[v], \tag{2.3.17}$$

and

$$\mathcal{F}[uv] = \mathcal{F}[u] \otimes \mathcal{F}[v]. \tag{2.3.18}$$

The operator $\otimes$ denotes the convolution operation.
Equation (2.3.18) is the frequency convolution and is known as a modulation. A wave can be modulated by varying its phase or its amplitude. Amplitude modulation is a well known technique in electronic communication such as signal transmission by a radio. On the other hand, phase modulation is mostly used in imaging techniques such as beam shaping [15]. Combination of both amplitude and phase modulation is called complex amplitude modulation [15]. Beam interaction with any optical element such as lenses or gratings can be described as a phase modulation.

Let $u_1 = u_{01}\, e^{i\phi_1}$ be the initial electric field of a light source and $u_2 = u_{02}\, e^{i\phi_2}$ be the final field after modulation of the initial field, where ϕ_1 and ϕ_2 are the phases. Modulation consists of finding the transfer function of the modulator field v given by

$$v = \frac{u_{02}}{u_{01}}\, e^{i(\phi_2 - \phi_1)}. \tag{2.3.19}$$

Stellenbosch University https://scholar.sun.ac.za

In cases where there is phase-only modulation, the amplitude of both fields are equal *i.e.* $u_{01} = u_{02}$. Thus, the phase of the modulator field is given by

$$\varphi = \mathrm{mod}(\phi_2 - \phi_1, \Upsilon), \tag{2.3.20}$$

where Υ is the period of the phase modulation (usually equal to 2π in most cases), and mod is the modulo operator. If the initial field has flat phase, then $\varphi = \mathrm{mod}(\phi_2, \Upsilon)$.

Amplitude modulation, on the other hand, consists of decreasing the amplitude of the light point by point by distributing it in different orders. By diffraction, the zeroth order does not contain any modulated light. Most of the modulated light goes to the first order. In that case, modulating the amplitude consists of distributing the undesired light onto the zeroth order or higher orders.

There is a device which is able to modulate the phase, and the amplitude of light in order to get a particular shape or to correct aberrations. It is called a spatial light modulator. This device can replace many optical elements. The next section gives an overview of its functionality and illustrates its usefulness for point spread function engineering.

Spatial light modulator

A spatial light modulator (SLM) is a liquid crystals (LC) microdisplay. LC is a particular class of molecules in which the liquid and crystal phases separated by at least one liquid crystalline phase. They are rod-like molecules, and have the mechanical properties of liquid, but behave optically like crystals [16]. There are two main types of LCs based on their structure: ferroelectric and nematic. Optical properties of LCs are modified by means of an applied electric field [17]. Ferroelectric and nematic LCs show an electric polarization which is a function of the strength of the applied electric field.

Nematic LCs are used more often compared to ferroelectric materials in the design of SLMs, because ferroelectric LCs have only two different molecular orientations and require high speed switching frequencies in the kHz range, which is not the case for a nematic LC. Their structure can be parallel or twisted and there is an orientation order of the molecules [16]. In twisted nematic LCs, molecules at one edge are typically oriented 90° about the orientation of the molecules on the other edge. The layers are parallel and share the same properties. When an electric field is applied, the nematic LC molecules tend to rotate from their initial orientation. The crystalline directions depend on the electric field applied on the LC molecules (Figure 2.7).

Nematic LCs hold the anisotropy properties of each molecule which results in a object with severe birefringence [16]. Birefringence means the refractive index varies as a function of the crystallographic directions. It has two refractive indices: the extraordinary refractive index n_e, and the ordinary refractive index

Stellenbosch University https://scholar.sun.ac.za

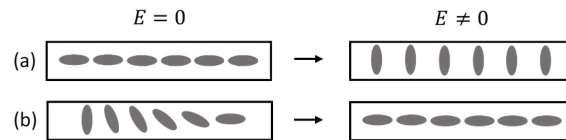

Figure 2.7: *Nematic liquid crystal microdisplay in a (a) parallel aligned structure and (b) twisted structure before and after an electric field is applied.*

n_o. Applying an external electric field over the LCs, therefore alters the birefringence by a specific amount allowing for programmable phase modulation. Furthermore, a liquid crystal spatial light modulator (LC-SLM) is polarization sensitive because of the molecular orientation of the LC modulation material.

Two addressing modes are available for controlling an incident beam, commonly referred to as the “read beam”. The first type of addressing mode is done optically. A control beam called “write beam” interferes with the “read beam”, and results in a new beam (Figure 2.8). The second addressing mode is done electrically where a particular phase mask, in form of an image, is computer generated. Each individual pixel of the phase mask is associated to an applied voltage on each cell of the LC [17]. The incident beam is then by transitivity changed using an electrical signal. The spatial light modulator used in this project uses this second mode where the LC layers are arranged on silicon substrate (LCOS) and on an electrically addressing mode. LCOS can be controlled from a computer [18].

A liquid crystal spatial light modulator works as an extended screen, a second monitor device. It is a pixelated display whose resolution depends on the total number of pixels. Each pixel can be manipulated independently. It modulates the phase or amplitude pixel by pixel. A phase mask is usually in the form of a 8-bit gray scale image loaded onto the SLM where black color corresponds to 0 phase and white, with 256 depth color, corresponds to 2π. Each gray level is associated to an increment of phase. One should be aware of the choice of the graphic format of the phase mask as it can affect the quality of the modulated beam. Images in .jpg format are more compressed than images in another format such as .png and .bmp. Their uses for modulation are not advisable.

The spatial light modulator’s efficiency is function of its fill factor, which is the surface area that can actively be used. The interpixel gap can be an origin of an undesired diffraction in the imaging process. That diffraction can be eliminated by loading a phase mask of a grating onto the SLM in order to separate the desired light in the 1st order from the 0th order, which is unmodulated (Figure 2.9).

Stellenbosch University https://scholar.sun.ac.za

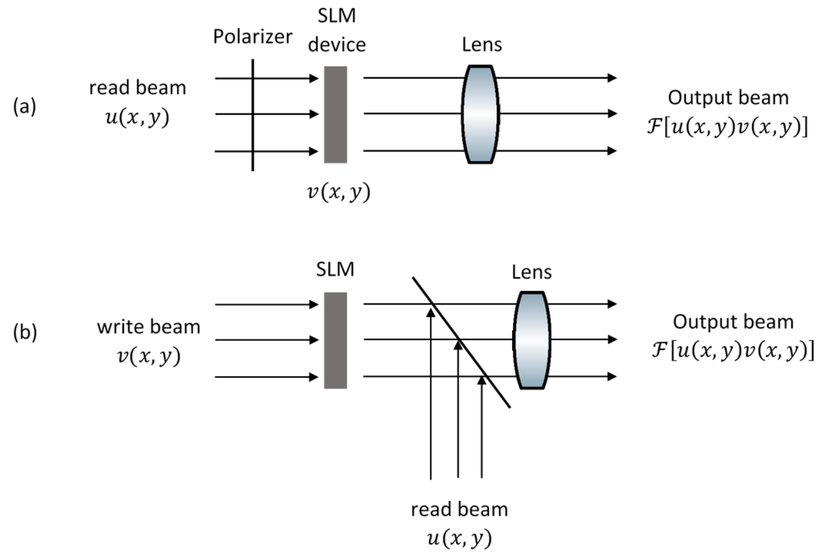

Figure 2.8: *Addressing mode: (a) Electrical. An electric field $v(x, y)$ with a particular phase mask is generated as image by a device connected to a computer and used to modulate the input field $u(x, y)$ (b) Optical. Modulation of the input beam $u(x, y)$ comes from an optical write-in image beam $v(x, y)$*

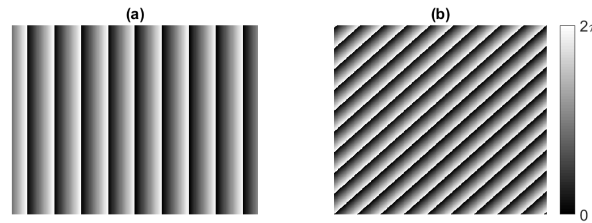

Figure 2.9: *A phase grating to improve the efficiency of an SLM. The role of a phase grating is to separate the modulated beam in the first order from the unmodulated light on the zeroth order. (a) Phase grating correcting the diffraction along the x-axis. (b) Phase for blazed grating correcting the diffraction in both directions x and y.*

The transfer function of a grating along the $x-$direction is given by

$$t = e^{2\pi i F_x x}, \tag{2.3.21}$$

where F_x is the grating frequency and x is the position along the $x-$direction. It follows the same for $y-$direction. The sum of the transfer function in both directions x and y corresponds to a blazed grating

$$t_\Sigma = e^{2\pi i (F_x x + F_y y)}. \tag{2.3.22}$$

One last parameter of a spatial light modulator that one should not neglect is its flatness. An SLM is not perfectly flat. For a LETO phase only spatial light

Stellenbosch University https://scholar.sun.ac.za

modulator, the peak valley value of the whole active area is (0.76 ± 0.11) μm whereas the peak valley value of a circle with radius 3.15 mm and same center as the active area is (0.19 ± 0.03) μm [18]. The flatness parameter of the SLM may be a cause of a certain aberration to the incident light. Therefore, distortions and aberrations must be taken into account and corrected if possible.

There are several factors that can affect the optical resolution of an imaging system. Even a point source cannot be imaged as it is, like a point at the image plane, but instead a point source is imaged like an Airy pattern, called the point spread function (PSF). We believe that modulating the phase of an emitter's PSF, using an SLM, can result an improved resolution, and provide a means to determine the three dimensional localization of an object as well as its orientation. A theoretical background of a PSF, followed by PSF engineering, is discussed in the following section.

2.3.3 Point Spread Function Engineering

A point spread function is the spread of a point source at the image plane. Differently stated, it is the image detected when observing a point source [4]. A 4f-type imaging system is used to illustrate this concept (Figure 2.10).

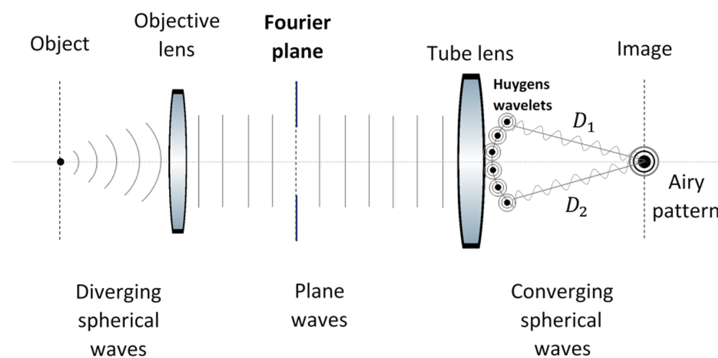

Figure 2.10: *Point Spread Function in a 4f-type imaging system. It images the spread of a point source at the image plane. This spreading can be understood by imaging the point object at the back focal plane of a tube lens following an objective lens.*

A point object is placed at the front focal point of an objective lens. It emits light in the form of diverging spherical waves. The waves propagate along the optical axis and are collected by the objective lens which transform the spherical waves onto plane waves. A tube lens, positive lens whose focal length is longer than the objective lens's focal length, is placed after the objective lens. The distance between the two lenses is set to be equal to the sum of their focal

Stellenbosch University https://scholar.sun.ac.za

lengths. As the tube lens collects plane waves, it is clear that it converges the waves at its back focal point.

According to the Huygens principle, each point of the converging spherical wave can be assumed to be a point source called a Huygens wavelet [11]. Huygens wavelets are coherent and synchronized, since they come from the same source. They interfere constructively with each other if the path lengths D_i and D_j for wavelet i and j respectively are multiple of the wavelength. However, they interfere destructively if the path length difference is of the form $(\frac{1}{2} + n)\lambda$, $n \in \mathbb{N}$ where λ is the wavelength.

Evaluating the interference at the focal plane of the tube lens enables one to get a successive pattern of dark and bright rings [11]. At the image plane, shown in Figure 2.10, a black color illustrates a constructive interference and white rings correspond to a destructive interference. Huygens wavelets interfere constructively more at the center due to the symmetrical nature of the spherical wavefront. The intensity of light is maximum at the center and is decreasing for further distance from the center.

Mathematically, the field of a PSF, evaluated at the distance r from the optical axis, is described by the Airy pattern whose function is given by the Bessel function of the first kind [4]

$$E(r) \propto E_0 \frac{\mathcal{J}_1(2\pi \sin\beta/\lambda)}{2\pi \sin\beta/\lambda}, \tag{2.3.23}$$

where E_0 is the amplitude of the electric field, $\mathcal{J}_1$ is the Bessel function of the first kind, β is the half of the opening angle of the tube lens, and λ is the wavelength of the light.

As the point object is moved forward or backward along the optical axis, the shape of the Airy pattern generally stays the same. However, if the phase of the light emerging from the point source is altered in someway, the Airy pattern itself could be altered as to give information of the object's position along the optical axis. This technique of altering the emitted light to gain unambiguous information is PSF engineering. The phase modulation technique, described in Section 2.3.2, is the method used for engineering a PSF. An SLM is placed at the Fourier plane, the back focal plane of the objective lens illustrated in Figure 2.10, and a specific phase pattern is loaded onto the SLM in electrical addressing mode.

An engineered PSF has a very important application in three-dimensional localization of single molecule and single particle tracking. The technique is used to recover inaccessible information such as the depth information and the orientation of an emitting dipole. The axial position of the molecule can be deduced from the shape of the point spread function. On the other hand, its intensity pattern is sensitive to its orientation. There are many PSF techniques for finding the axial localization and the orientation of a single molecule such as

Stellenbosch University https://scholar.sun.ac.za

the double helix PSF [19], astigmatism PSF [20], corkscrew PSF [21], tetrapod PSF [22], and pyramidal PSF [23]. Each of those PSFs behave differently as the focus and defocus of the PSF is changing. The main focus of this project is to study the double helix PSF, because of its ability to give an accurate localization for axial position and orientation of a single molecule.

2.3.4 Double helix point spread function (DH-PSF)

A DH-PSF is a three-dimensional rotating point spread function. It exhibits two lobes which are able to rotate about the optical axis under defocus. Also, the number of photons in each lobe and the lobe asymmetry lead to gaining information of the orientation of the point source.

Phase mask design

The phase mask for generating a DH-PSF consists of a superposition of vortex point spread functions. It is a combination of a given number N of annular Fresnel zones. The phase mask is characterized by the number of rings and its outer radius r_{mask}. The $m-$th ring, $m \in \mathbb{N} \cup [2, N]$, is bounded by circles of radius r_{m-1} and r_m, where the outer radius of the $m-$th ring is $r_m = r_{\text{mask}} \left(\frac{m}{N}\right)^\tau$, $\tau \in \mathbb{Q}$. The first ring is a disk with radius equal to $r_{\text{mask}} \left(\frac{1}{N}\right)^\tau$ [19].

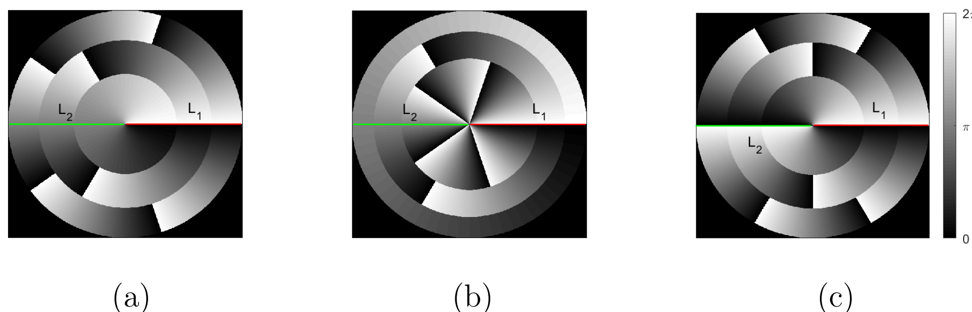

(a) (b) (c)

Figure 2.11: *Phase mask for generating a DH-PSF. A phase mask of a DH-PSF is a superposition of vortex-PSFs in a particular configuration which consists of an order of the rings, and an existence of two lines, L_1 and L_2, with same gray phase values (green and red). (a) and (c) allow to get a DH-PSF, but (b) will not give a DH-PSF.*

Physically, a superposition of vortex-PSFs is described by the interference of the vortex-PSFs. The phase of a vortex is given by

$$P(h) = h\phi, h \in \mathbb{Z}^*, \tag{2.3.24}$$

where ϕ is azimuthal angle and h is helical charge.

Stellenbosch University https://scholar.sun.ac.za

The transfer function of the vortex-PSFs is then as follows

$$t(h) = e^{iP(h)}\,\zeta(\rho), \tag{2.3.25}$$

where $\zeta(\rho)$ is a circular function equal to 1 if ρ belongs to the phase ring region and 0 otherwise.

In order to visualize the intensity pattern for the above mentioned transfer function, let us first consider the two distinct phase patterns which are illustrated in Figure 2.11. The two phases 2.11(a), and 2.11(b) each have three phase rings with helical charges $1, 3$, and 5. The phases 2.11(a), and 2.11(b) differ by the radius of each ring containing the helical charges $1, 3$, and 5. The field from each phase ring are evaluated. Let $t_m(h)$ denote the transfer function of ring m with helical charges h. The interference of the three fields with transfer functions $t_1(1), t_2(3)$, and $t_3(5)$ are evaluated at the focal plane. The total field is given by the sum

$$t_\Sigma = t_1(1) + t_2(3) + t_3(5). \tag{2.3.26}$$

The intensity pattern at the focal plane is given by the amplitude of the Fourier transform of t_Σ. On one hand, the intensity pattern, which corresponds to the phase mask illustrated in Figure 2.11(a), is shown in Figure 2.12. We see that as the helical charge is increasing with the outer radius of the ring, the diameter of the intensity pattern of each field is expanding and we get a double lobe.

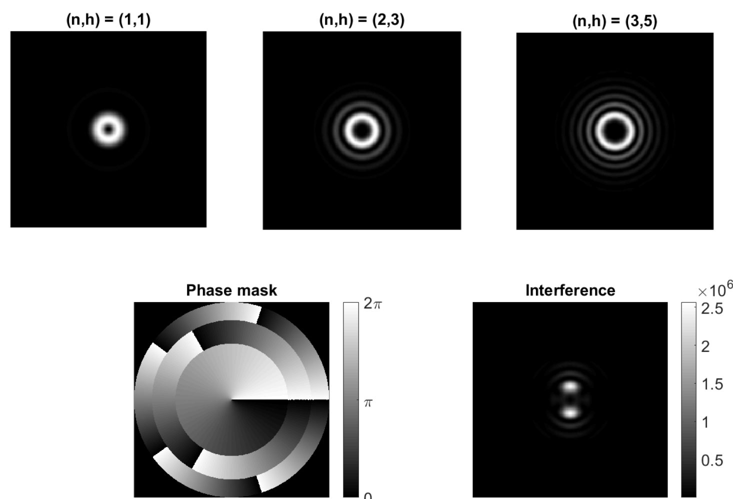

Figure 2.12: *Intensity pattern of a DH-PSF formed with a phase pattern composed by three rings with helical charges* $1, 3$, *and* 5. *The interference of the transfer functions of three rings with increasing helical charge and outer radius permits to get a double-lobbed pattern. The smallest ring is with one helical charge, second ring with three helical charges, and the largest ring with five helical charges.*

Stellenbosch University https://scholar.sun.ac.za

On the other hand, if we reverse the order of the rings, *i.e.* the smallest ring is with a higher helical charge (Figure 2.11(b)), the double lobe shape is not obtained (Figure 2.13). A ring with higher helical charge requires higher numerical aperture to focus. That means, an higher helical charge should be associated to a bigger outer radius in order to get a double-lobbed pattern.

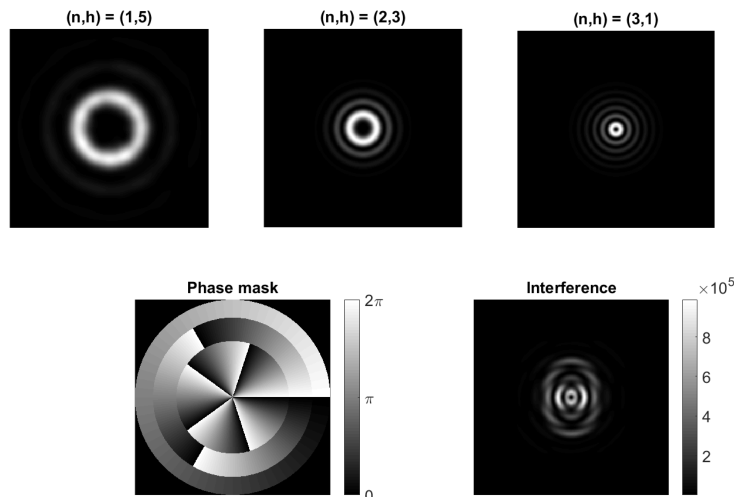

Figure 2.13: *Intensity pattern of an engineered PSF formed with a phase pattern composed by three rings with helical charges* $5, 3,$ *and* 1 *respectively. A ring with higher helical charge requires higher numerical aperture to focus. As the smallest ring is with five helical charges, the second ring with three helical charges, and the largest ring with one helical charge, a different PSF from a DH-PSF is obtained by interference of the transfer functions of the three vortex-PSFs.*

An effective phase mask for DH-PSF therefore depends on the size of the outer radius r_m of each optical vortex. The size of r_m is function of the exponent parameter τ (described earlier in the first paragraph of this section). The common rotation, hence the rotational rate α of the DH-PSF is a result of any change in the exponent τ in each ring. Furthermore, it is related to the phase offset Ψ_m that each ring m of the phase mask experiences under defocus due to a lens:

$$\alpha_m = \frac{\Psi_m}{m}. \tag{2.3.27}$$

The phase offset, Ψ_m, is proportional to the squared outer radius, r_m^2, of each ring [19]. As a result, the rotational rate of the ring m is given by

$$\alpha_m = r_{\text{mask}}^2 \left(\frac{m}{N}\right)^{2\tau} \frac{1}{m}. \tag{2.3.28}$$

If $\tau = \frac{1}{2}$, the rotation that each ring experiences is independent of its index, m. That yields to a rotational invariance of the rotational rate, α, of the DH-PSF

Stellenbosch University https://scholar.sun.ac.za

$$\alpha = \frac{r_{\text{mask}}^2}{N}. \tag{2.3.29}$$

However, the two lobes are not compact comparing to the case where $\tau = \frac{3}{4}$, as seen in Figure 2.14. In this second case, the rotational rate is dependent of the ring index, m, but the two lobes are more intense and compacts.

Figure 2.14: *Comparative images for different τ parameter. Left hand side and right hand side correspond to $\tau = \frac{1}{2}$ and $\tau = \frac{3}{4}$ respectively.*

The exponent τ plays an important role in the compactness of the two lobes. $\tau = \frac{1}{2}$ is advisable if the imaging system requires an invariant rotation, but $\tau = \frac{3}{4}$ is better if compact lobes are needed.

Alternatively, although the phase mask illustrated in Figure 2.11(c) also permits to get a DH-PSF, the intensity profile of the double lobes patterns is slightly different from the one generated from the phase mask in Figure 2.11(a) (Figure 2.15).

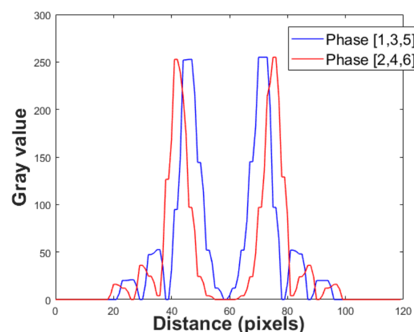

Figure 2.15: *Image comparative of the double lobes intensity profile generated from a phase mask with helical charges* $[1, 3, 5]$ *and* $[2, 4, 6]$.

The distance between the two peaks of the double lobes using the phase with helical charges $[2, 4, 6]$ in 2.11(c) is larger than the one using 2.11(a). For this reason, the location of the double lobes corresponding to $[2, 4, 6]$ can be achieved accurately than the ones corresponding to $[1, 3, 5]$. However, the intensity of the two peaks for $[2, 4, 6]$ are lower compared to the intensity of

Stellenbosch University https://scholar.sun.ac.za

the two peaks for $[1, 3, 5]$. Use of the phase mask with helical charges $[1, 3, 5]$ is therefore more advantageous in photon-limited imaging.

A simulation of an imaging using a DH-PSF engineering is developed in the next section.

DH-PSF for a single radiating dipole

In this section we apply the DH-PSF phase mask to the emission of a radiating dipole through simulation in order to illustrate the rotational behaviour of the PSF. The intrinsic benefit of this DH PSF will be discussed in Chapter 4. Assume the dipole is oriented along the unit vector $\widehat{\eta}$ and emits light in $\widehat{r}$ direction (Figure 2.16).

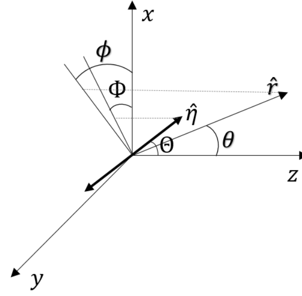

Figure 2.16: *Dipole orientation.*

The dipole, acting like a point source, is initially placed at the front focal plane of an objective lens, with focal length equal to $f_1 = 20$ cm (Figure 2.17), of a $4f-$type imaging, where the optical axis is along the $z-$axis.

The electric field of a dipole radiation at the focus is given in terms of the Green's function by Equation (2.2.25). As long as the dipole is moved forward or backward by a distance d, the system is under defocus, and the field experiences an additional phase factor $nkd\cos\theta$ where $k = \frac{2\pi}{\lambda}$ is the wavenumber, λ is the wavelength [23], and n is the refractive index of the medium where the dipole is embedded. The field then becomes

$$\overrightarrow{E}_{\text{obj}}(\theta, \phi, d) = Ae^{inkd\cos\theta} \frac{e^{inkr}}{4\pi r} \left(\overline{I} - \frac{rr^{\dagger}}{r^2} \right) \overrightarrow{\eta}, \tag{2.3.30}$$

where A is a constant,

$\overrightarrow{r} = \begin{pmatrix} \sin\theta\cos\phi \\ \sin\theta\sin\phi \\ \cos\theta \end{pmatrix}$ is the vector propagation and r is its magnitude,

$n = 1.5$ is assumed to be the value of the refractive index of the medium between the sample and the objective, which is the dipole's embedding media

Stellenbosch University https://scholar.sun.ac.za

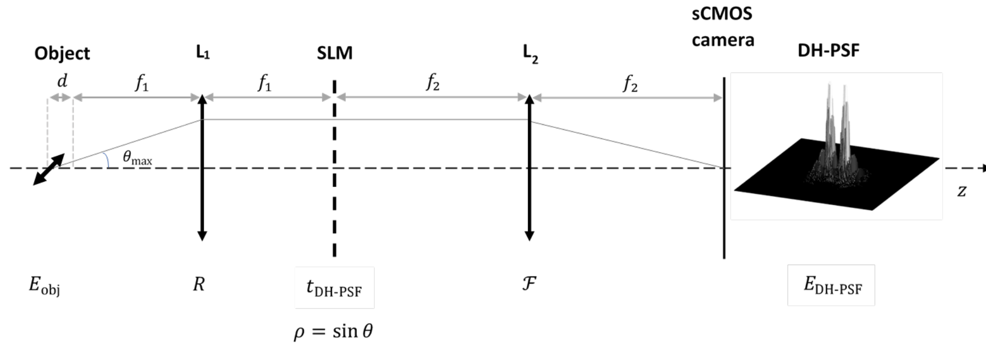

Figure 2.17: *Schematic representation of the 4f imaging system employed to investigate the single dipole DH-PSF. The emitter is initially placed at the focal point of an objective lens L_1. L_1 acts as a rotation matrix denoted by R. The axial position of the dipole is defined by the defocus distance d. A non-zero value of d causes an additional phase on the electric field of a dipole emitter. An SLM is set at the back focal plane of L_1 to modulate the phase of the emitted light. The 3D electric field E_{obj} is projected onto the surface plane of the SLM by setting $\rho = \sin\theta$. A second lens L_2 with focal length $f_2 > f_1$ serves to complete the modulation.*

and the immersion oil,
$\overline{I} = \begin{pmatrix} 1 & 0 & 0 \\ 0 & 1 & 0 \\ 0 & 0 & 1 \end{pmatrix}$ is the unit dyadic.

The objective lens L_1 is a thin lens and can only collect light within a circular region limited by the polar angle $\theta_{\max}$, derived from the relation $\mathrm{NA} = n \sin\theta_{\max}$, where NA is the numerical aperture of the microscope objective, and n is the refractive index above mentioned. In our simulation, NA is set to be 1.3. The distance d is in order of μm and assumed to be small compared to the focal length $f_1 = 20$ cm. Therefore, we assume that the rays collected by the lens become parallel at the back focal plane of L_1. Thus, L_1 acts mathematically like a rotation matrix [23] defined by

$$R = \sqrt{\frac{n}{n_0 \cos\theta}} \begin{pmatrix} \cos(\theta) - \sin^2(\phi)(\cos\theta - 1) & \sin(2\phi)(\cos(\theta) - 1)/2 & -\cos(\phi)\sin(\theta) \\ \sin(2\phi)(\cos(\theta) - 1)/2 & 1 - 2\sin^2(\frac{\theta}{2})\sin^2(\phi) & -\sin(\phi)\sin(\theta) \\ \cos(\phi)\sin(\theta) & \sin(\phi)\sin(\theta) & \cos(\theta) \end{pmatrix}, \quad (2.3.31)$$

where n_0 is the refractive index at the back focal plane and set to be equal to the refractive index of air.

In addition, the emitted light propagates along the focal length distance f_1. The field at the back focal plane becomes

$$\overrightarrow{E}_{\mathrm{bfp}}(\theta, \phi, d, f_1) = \frac{e^{inkf_1}}{4\pi f_1} R \overrightarrow{E}_{\mathrm{obj}}(\theta, \phi, d). \quad (2.3.32)$$

Stellenbosch University https://scholar.sun.ac.za

The SLM has plane surface and can only modulate field in two dimensions. Hence, we set $\rho = \sin\theta$ which yields to the projection of the 3D electric field onto a surface plane at the back focal plane. The intensity pattern at the back focal plane is therefore

$$I_{\text{bfp}}(\rho, \phi, d, f_1) = \overrightarrow{E}_{\text{bfp}}(\rho, \phi, d, f_1) \cdot \overrightarrow{E}_{\text{bfp}}(\rho, \phi, d, f_1)^{\dagger}. \tag{2.3.33}$$

The intensity pattern is function of the orientation of the dipole emitter. Figure 2.18 shows the intensity pattern, evaluated at the back focal plane, within different dipole orientations.

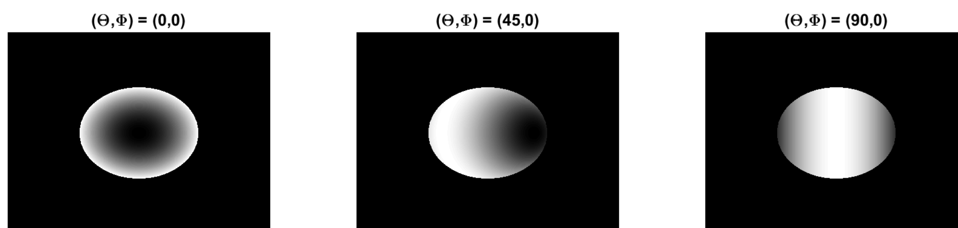

Figure 2.18: *Intensity pattern of the field from a dipole emitter with different orientations evaluated at the back focal plane. It is function of the polar and azimuthal angle of the dipole moment.*

As the SLM can only modulate a specific polarization state, the incident field is separated into a horizontal and a vertical polarized state. The second lens, L_2, serves to complete the modulation. It acts as a Fourier transform as it relays the intermediate image placed at its front focal plane (Fourier plane) to its back focal plane (image plane). The focal length of L_2, f_2, should be larger than the focal length of the objective lens to ensure that the magnification $M = \frac{f_2}{f_1}$ of the system is bigger than 1.

Therefore, the electric field at the image plane is given by

$$\overrightarrow{E}_{\text{DH-PSF}} = \mathcal{F}[\overrightarrow{E}_{\text{bfp}}(\rho, \phi, d, f_1)\; t_{\text{DH-PSF}}(\rho, \phi)], \tag{2.3.34}$$

where

$$t_{\text{DH-PSF}}(\rho, \phi) = e^{iP_{\text{DH-PSF}}(\rho,\phi)} \times \zeta(\rho), \quad \zeta(\rho) = \begin{cases} 1 & \text{if} \quad \rho < \sin\theta_{\max}, \\ 0 & \text{otherwise} \end{cases} \tag{2.3.35}$$

is the transfer function of the modulator field loaded on the SLM. $P_{\text{DH-PSF}}$ is the phase illustrated in Figure 2.11(a).

The intensity pattern at the image plane is given by

$$I_{\text{DH-PSF}} = \overrightarrow{E}_{\text{DH-PSF}} \cdot \overrightarrow{E}^{\dagger}_{\text{DH-PSF}}. \tag{2.3.36}$$

Stellenbosch University https://scholar.sun.ac.za

A rotating DH-PSF is computationally simulated in the horizontal (H) and vertical (V) channels over a depth range equal to 1.4 μm. The emission wavelength is set to be equal to 550 nm and the dipole is oriented with $(\Theta, \Phi) = (45°, 90°)$ for this particular simulation. For the simulation, instead of rotating and reflecting the field on the vertical channel, rotating the phase mask displayed on that channel seems more efficient (Figure 2.19).

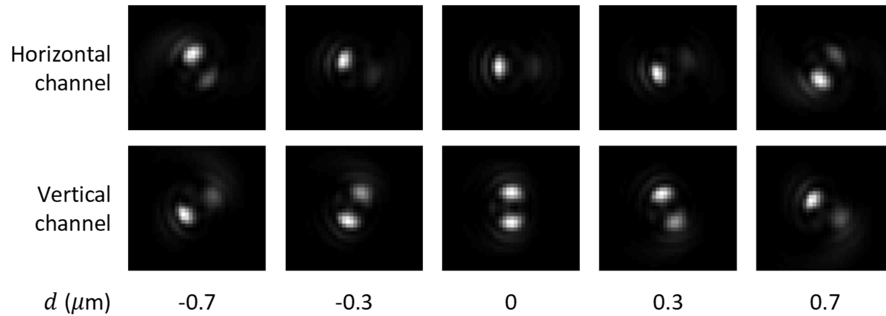

Figure 2.19: *Simulated DH-PSF for a dipole oriented with* $(\Theta, \Phi) = (45°, 90°)$ *and emitting light with wavelength* $\lambda = 550$ *nm. H and V denote the horizontal and vertical channel respectively. The center value corresponds to a distance* $d = 0$*. The system is at focus at that position.*

An emitter does not always behave like a dipole. It can radiate uniformly in all directions, which means it does not have any orientation. Such type of emitter is isotropic, and its radiation propagation can be modelled using the sum of the radiation from three orthogonal dipole superimposed [23]. The experimental validation of what has been discussed theoretically in this section will be developed in the next sections.

Stellenbosch University https://scholar.sun.ac.za

Chapter 3

Experimental setup

This chapter describes the apparatus and the experimental setup for modulating the phase of an emitter's light in order to track the emitter in three dimensional space. The first section gives an overview of the sample preparation and description. The sample is optically excited with a solid-state laser with wavelength 532 nm in an inverted wide-field microscope and the fluorescence emission is imaged through a 4f-type imaging setup coupled to a sCMOS digital camera. A piezoelectric stage with nanometer positional accuracies is attached to the microscope to control the defocus and focus, hence axial position, of the emitter.

3.1 Sample description

It is required for an emitter object to be bright enough to get an accurate localization of its position. The brightness and photostability of nanoparticles have been proved to be higher compared to other fluorescent molecules photostabilities [3]. The improved brightness and photostability of fluorescently labelled nanoparticles (NP) versus single fluorescent molecules is expected as each NP generally has a large number of fluorescent molecules attached to it. For this reason it was decided to initially concentrate on the localization of NPs. This section presents the sample preparation, and gives an overview of the analysis of the photostabilities of the NPs.

3.1.1 Sample preparation

Three types of NPs are used in this work: 50 nm diameter fluorescent silica NPs (Sigma Aldrich 797952), 300 nm and 600 nm polymer based NPs (obtained from Prof Bert Klumperman Group, Stellenbosch University) which are believed to have cross linked centers which give rise to strong fluorescence throughout the visible spectrum. The NPs are typically embedded in a thin layer polymer on a glass cover slide. The polymer's refractive index

Stellenbosch University https://scholar.sun.ac.za

should be approximately the same as the refractive index of the immersion oil ($n_{\text{oil}} = 1.518$) and glass slide ($n_{\text{glass}} = 1.5$) of the microscope to avoid unnecessary aberrations, and to maintain high optical throughput. Polystyrene is used as embedding media as it has a refractive index equal to 1.598 at the excitation wavelength. [24].

The sample preparation starts by cleaning the cover glass slide on which the sample will be spin coated. The cover glass slide with dimension 22×22 mm is cleaned to eliminate all the impurities which may affect our sample. For this purpose the cover glass slide is submerged into a concentrated (300 mg/mL) solution of KOH (potassium hydroxide) dissolved in 95% ethanol and allowed to sonicate for 10 mn at a temperature of 30°C. Distilled water is used to rinse the cover slide afterwards.

The procedure of spin coating of NPs with polystyrene is done by following three steps. The first step consists of mixing a solution of NPs in a given solution of polystyrene. The concentration must be low enough to avoid any overlap of NPs when imaging the sample. The solvent used to dissolve the NPs and the embedding media must be the same. Here, toluene is used as NPs solvent and polymer solvent. In the second step, the NPs and polystyrene mixture is sonicated for few minutes at 30°C to ensure that they are well mixed. The last step is to drop a necessary volume (roughly 15 μL) of the mixture onto the cleaned cover slide mounted on a spin coater device which spins the slide at roughly 2000 rpm for 1 mn.

3.1.2 Nanoparticle's photostabilities

A NP's photostability is defined by its photoblinking and its ability to resist to photobleaching when illuminated. However, of primary concern in this work is the rate at which these NPs photobleach as this ultimately influences the localization accuracy.

Assuming a mono-exponential decay in the fluorescence emission of a NP due to photobleaching yields the following expression:

$$I(t) = I(0)\exp(-\gamma t), \tag{3.1.1}$$

where I(t) is the fluorescence intensity at a given time t, $I(0)$ the fluorescence intensity at time $t = 0$, and γ the decay rate (bleaching rate).

As mentioned before, the photobleaching process affects the accuracy of the localization of the emitter. Therefore, knowledge of γ is pivotal and allows us to get an effective range of operation time of our sample. Figure 3.1 illustrates the photobleaching behaviour of the 50 nm NPs captured using the experimental setup (see Section 3.2) designed for this work. Photons emitted from the NPs are collected and imaged on an sCMOS camera every 500 ms. The sum of the pixels values in a region of interest of the image of the nanoparticle is assumed

Stellenbosch University https://scholar.sun.ac.za

to be the number of photons collected by the camera. The background is subtracted and the result is plotted in Figure 3.1.

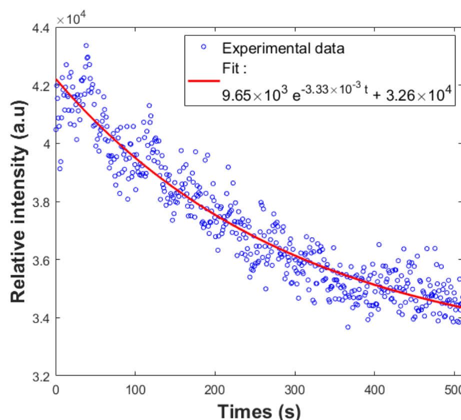

Figure 3.1: *Photobleaching decay of a 50 nm fluorescent silica nanobead. The number of photons emitted by a nanoparticle is decreasing exponentially over its exposure time. The solid red line is the model function of the experimental data points in blue.*

Using the photobeaching model in Equation (3.1.1), it was determined that the photobleaching rate is $3.33 \times\ 10^{-3}$ the inverse thereof gives the bleaching time constant of about 300 s, which suggests that consecutive measurements should be kept far below 5 mn. In this work, the typical measurement time was about one minute.

The next paragraph develops the elements of the apparatus for imaging the NPs.

3.2 Imaging system

This section describes the experimental setup for imaging NPs in an inverted wide-field fluorescence microscopy. A spatial light modulator (SLM) is placed in the pathway of a 4f-type imaging system to modulate the phase of the fluorescent light emitted by the NPs.

3.2.1 Experimental apparatus

The experimental setup is illustrated in Figure 3.2.
The sample, spin coated on a cover slide, is placed on a holder above the microscope objective (100X Nikon Plan Fluorite Oil Immersion Objective, NA 1.3). The microscope objective is housed in a nano-positioning piezoelectrically driven holder, which is mounted on a re-purposed Zeiss Axiovert 100

Stellenbosch University https://scholar.sun.ac.za

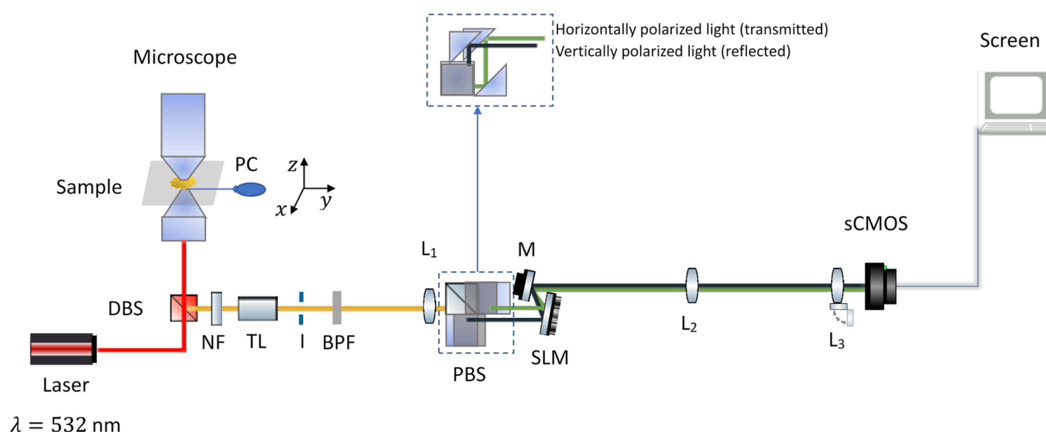

Figure 3.2: *Schematic diagram of experimental setup. PC: piezo controller controlling the axial position of the sample along the $z-$axis. DBS: dichroic beam splitter reflecting the fluorescence light and transmitting the excitation source $\lambda = 532$ nm. NF: notch filter 532 nm. TL: tube lens. I: iris. BPF: bandpass filter with center wavelength 565 nm and bandwidth 24 nm. L1, L2, L3: converging lenses with focal length $f_1 = 200$ mm, $f_2 = 300$ mm, $f_3 = 60$ mm respectively. PBS: polarizing beam splitter encountered by four right angled prism mirrors. M: flat mirror. SLM: phase only spatial light modulator. sCMOS: digital camera.*

microscope. This piezoelectrically driven holder allows for easy image focusing and defocusing. The positioning control is done with custom LabVIEW code where position feedback and subsequent calibration is achieved through implementing a home-built Michelson interferometer setup (see Section 3.3 for more details).

The excitation source is a diode pumped solid state laser (Oxxuis, LCX-532L) with wavelength $\lambda = 532$ nm with an output power of 518 mW. Light propagates through a collection of lenses and diffusers (not shown on Figure 3.2) as well as a dichroic beam splitter (DBS) before reaching the sample. The collection of lenses and diffusers ensures a wide-field illumination with a typical on sample intensity of 500 kW/m^2.

The DBS separates the fluorescence emission from the excitation source. In this setup, the excitation light is transmitted whilst the back-propagating (with respect to the excitation light) fluorescence emission from the sample is reflected. However, the DBS is not 100% effective, as a result some of the laser light is also reflected. For this reason, a notch filter (Thorlabs, NF533-17) with blocking wavelength 532 nm and bandwidth of 17 nm is placed after the DBS to illuminate background laser light. Apart from an infinity corrected microscope objective, a paired tube lens (Thorlabs, TTL200) is placed at an appropriate distance after the notch filter. An intermediate image of the sample is then

Stellenbosch University https://scholar.sun.ac.za

formed at a position indicated by an iris.

The iris is used to limit the field of view. The maximum aperture thereof is 25 mm. The numerical aperture of the microscope is constant, but is reduced by closing the iris aperture. Reducing the field of view increases the image contrast by eliminating some of the out of focus light. After propagating through the iris, the light passes through another bandpass filter (Thorlabs, MF565-24), and then through a first converging lens L1 with focal length $f_1 = 200$ mm placed a distance exactly f_1 after the iris.

The fluorescent light is then separated into horizontally and vertically polarized orientations by a polarizing beam splitter (PBS). The horizontally polarized light is transmitted whereas vertically polarized light is reflected. The vertically polarized light is required to be parallel to the horizontally polarized light, such that the SLM (which can only address one polarization direction) imparts the correct phase onto the light. To achieve this, four right angled prism mirrors (Thorlabs, MRA25-E02) are placed in such a way as to rotate the polarization of the reflected light. The light from the two separated paths are guided to a SLM (Holoeye, LETO phase only SLM) placed a distance f_1 from lens L1.

The SLM is a display device and is connected to a computer in extended monitor (1920 $\times$ 1080 pixels) mode. Its pixel pitch and addressing bit depths are 6.4 μm and 8 bits respectively. This specific SLM can only modulate the phase of light within wavelength range 400 to 1100 nm [18]. The advantage of this SLM is its fill factor, surface area which can actively be used. The fill factor is 93%. The average reflectivity of this SLM is 75%. The unwanted intensity of the 0th order is also reduced with a diffraction efficiency of more than 80%. Hence, the total light efficiency is about 60% using this SLM. After interacting with the SLM, the light from the two separate paths are reflected onto a second lens L2 by a flat mirror, M.

The converging lens L2 with focal length f_2 is placed a distance f_2 from the SLM. At this point, the light is either sent directly to the scientific grade sC-MOS camera (Hamamatsu Photonics, C11440-22CU) for imaging the sample plane or first sent through a third lens L3 ($f_3 = 60$ mm) and then onto the camera in order to image the phase mask on the SLM.

As a result of the collection of lenses and the complicated optical geometry used in the system, it is practically more advisable to determine the overall magnification through appropriate experiments. This involves imaging an object with known dimensions and determining a so called image calibration factor.

Stellenbosch University https://scholar.sun.ac.za

3.2.2 Imaging calibration factor

The calibration factor of our setup is achieved by imaging a USAF 1951 test target (Thorlabs, R3L1S4P). The test target is placed at the exact same position as the sample described in the previous section. The target consists of dark lines in a horizontal and vertical pattern with a clear background. The vertical and horizontal lines are sub-divided into 6 groups with different line spacing.

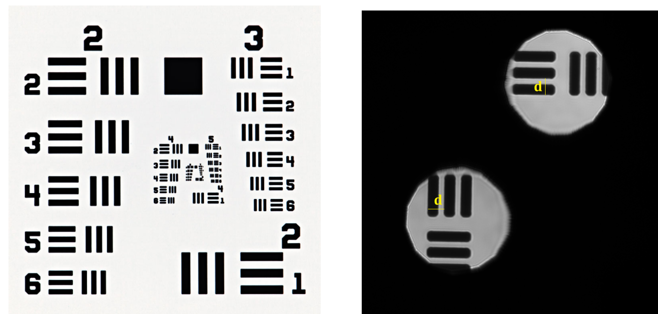

Figure 3.3: *Use of the USAF 1951 test target for finding the imaging calibration factor. Left hand side: The USAF 1951 test target. The numbers aligned horizontally denote the group whereas the increasing numbers along the vertical axis are elements of the group. Each group is associated to a particular resolution. The background is clear for a positive USAF 1951 (Image source: Thorlabs). Right hand side: element 6 of group 7 is the smallest pattern of the target imaged in vertical channel (upper disk) and horizontal channel (lower disk). d is the size of a line pair.*

The resolving power and magnification of the system is determined by identifying and imaging each line pair in a group of the pattern. A line pair is defined as the thickness of a dark line plus the thickness of its adjacent bright line. A bright line here means the distance between two dark lines and has the same thickness as a dark line. Using knowledge of the line pair together with the experimentally obtained image thereof (Figure 3.3 right) both the overall magnification and image calibration factor is calculated.

Therefore, let d_i and d_o be the size of one line pair in image plane and in object plane respectively. The distance d_i is expressed in terms of pixels in image plane and d_o is in terms of resolution line pair per millimeter. In order to determine the magnification, both d_i and d_o must have the same unit. Thus,

$$d_i = n_p \times s_p \quad \text{and} \quad d_o = \frac{1}{r}, \tag{3.2.1}$$

where n_p : number of pixels for a line pair in image plane,
s_p : the pixel size, equal to 6.5 μm for our system,
r : resolution factor in line pair per millimeter (lp/mm) and differs for each

Stellenbosch University https://scholar.sun.ac.za

element of each group. Its value is equal to 228 lp/mm for the smallest element 6 of group 7.

The magnification of the imaging is given by $M = \frac{d_i}{d_o}$. Its value is approximately equal to 161 for our system. Theoretically, the magnification of a $4f-$type imaging is equal to $M = \frac{f_2}{f_1} = 150$ where $f_1 = 200$ mm and $f_2 = 300$ mm are the focal length of the achromatic lenses L1 and L2 described previously.

Finally, we define the calibration factor C to be the size of the object imaged per pixel:

$$C = \frac{d_o}{n_p}, \tag{3.2.2}$$

C is approximately equal to 40.22 nm/pixel for our system. The knowledge of C factor allows us to identify whether we are imaging only one NP or not. However, the smallest distance we can image is still diffraction limited. Furthermore, the image calibration factor is used to map images to the "real" two dimensional space (lateral space). Information of the third dimension (axial) is obtained through engineering the phase of the single emitters. Still in order to quantify the axial position of an emitter, it is required to have appropriate nano-positioning capabilities.

3.3 Axial positioning

A piezoelectric stage in conjunction with a home-built Michelson interferometer setup is used in this project to verify and quantify axial translations.

Figure 3.4 shows a picture of the interferometer developed for this project. The light source is a laser diode with center wavelength $\lambda = 854.3$ nm. Mirrors M1, M2, M3 and M4 are mounted on compact kinematic mirror mounts permitting them to be adjusted such that the light follows the right path and that the amount of light reaching mirrors D1 and D2 have equal intensities. The position of D2 is controlled by a piezoelectric stage as it is directly mounted to it. It can move up or down depending on the applied voltage.

When a voltage is applied on the piezo, the D2 mirror moves and causes a path length difference between the reflected light from D1 and D2. Hence, a shift is noticed in the interference pattern imaged on the digital camera. To understand the origin of the interference pattern and the shift as well as how this is used to determine the amount by which the piezoelectric stage moved, the scalar addition of the monochromatic reflected beams from D1 and D2 will be considered.

Let $E_1 = E_{01} \exp\left[i(k_1 r - wt + \phi_1)\right]$ and $E_2 = E_{02} \exp\left[i(k_2 r - wt + \phi_2)\right]$ be the reflected electromagnetic waves from D1 and D2 respectively, where E_{01} and E_{02} are the amplitudes, w is the angular frequency, $k_1 = k_2 = \frac{2\pi}{\lambda}$ is the

Stellenbosch University https://scholar.sun.ac.za

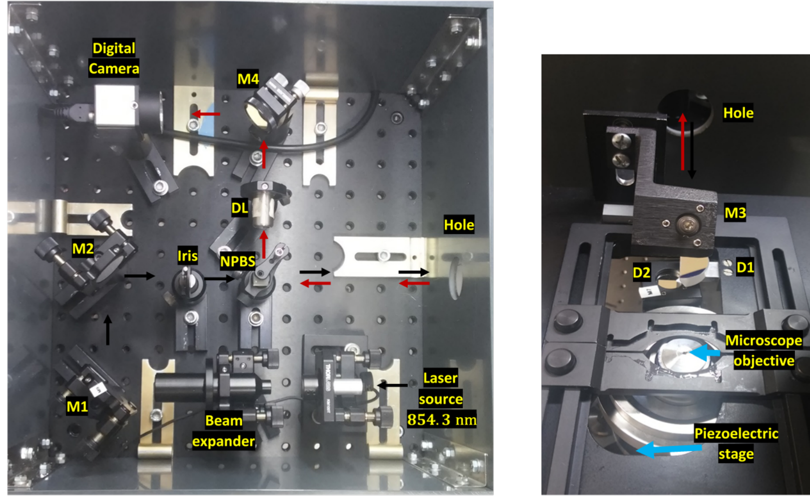

Figure 3.4: *Michelson interferometer for measuring optical pathlength difference between two mirrors D1 and D2. M1, M2, M3, are M4 are mirrors for reflecting light. The iris serves to reduce the diffraction and to focus the light onto the non polarizing beam splitter (NPBS). DL is a diverging lens.*

wavenumber, λ is the wavelength of the light source, r is the propagation distance of light, and ϕ_1 and ϕ_2 are additional phases. Since the amount of light distributed on the two mirrors are experimentally set to be equal, we assume that $E_{01} = E_{02} = E_0$. The superposition of those two fields, E_1 and E_2, gives the interference pattern on the image plane which is described by E_{tot}:

$$\begin{aligned} E_{\text{tot}} &= E_1 + E_2 \\ &= E_0 \exp[i(kr - wt)] \left(\exp[i\phi_1] + \exp[i\phi_2]\right). \end{aligned} \tag{3.3.1}$$

The time-average intensity of some position r of the superposition is given by the modulus square of the total electromagnetic field and can be expressed as follows:

$$\begin{aligned} I_{\text{tot}} &=< E_{\text{tot}} \cdot E^*_{\text{tot}} > \\ &=< E_0 \cdot E^*_0 > \left(\exp[i\phi_1] + \exp[i\phi_2]\right)\left(\exp[-i\phi_1] + \exp[-i\phi_2]\right) \\ &= I_0 \left(2 + \exp[-i\delta] + \exp[+i\delta]\right), \text{ where } \delta = \phi_2 - \phi_1 \\ &= 2I_0(1 + \cos\delta) \\ &= 4I_0 \cos^2\left(\frac{\delta}{2}\right). \end{aligned} \tag{3.3.2}$$

The intensity is maximum and the interference is constructive if $\delta = \pm 2m\pi, m \in \mathbb{N}$. Destructive interference occurs when $\delta = \pm(2m+1)\pi, m \in \mathbb{N}$. The phase parameter δ therefore controls the amount of interference, and for the setup

Stellenbosch University https://scholar.sun.ac.za

is thought of as the phase difference of light reflecting of D1 and D2. As the mirrors move with respect to one another this phase difference changes and results in a shift in the interference pattern. It is a shift parameter.

The calibration factor of the piezoelectric system consists of finding the phase shifting per volt applied to the piezoelectric stage.

Five images of interference pattern of the two beams reflected from the two mirrors D1 and D2 are collected and averaged after every 1 V increase applied to the piezo. The intensity of the interference pattern for a given applied voltage is fitted with a model function y_V given by

$$y_V = A\cos^2(\frac{2\pi}{\lambda}x + \delta_V) + B, \tag{3.3.3}$$

where A represents the amplitude, $\frac{2\pi}{\lambda}x$ is a constant phase change in time, δ_V is the phase shifting of the interference pattern and B is baseline, a vertical offset.

The Levenberg Marquardt algorithm for nonlinear least square curve[1] fitting described in [25] is used to minimize the error between model function and data such that the model parameters A, λ, δ_V, and B can be extracted.

The choice of the initial guess of the parameters for a fit function model is very important. The initial guess for the amplitude is the maximum value of the intensity whereas the baseline is initially set to be the minimum value. The wavelength, λ, is initially assumed to have the same value, 854.3 nm, as the diode laser wavelength. The guess for the phase shifting δ is achieved by doing a pattern matching. This last consists of finding δ such that $|y(x =$

[1] The Levenberg Marquardt method is a combination of the gradient descent method and the Gauss-Newton method. It minimizes the sum of squared errors, $\chi^2(p) = \sum_{j=1}^{m}\left[\frac{y(t_j)-f(t_j,p)}{\sigma_{y_j}}\right]^2$, by solving the following equation in terms of the perturbation factor h_{lm} [25]

$$\left[J^T W J + \vartheta I\right] h_{lm} = J^T W(f(p) - y), \tag{3.3.4}$$

where $\{(t_j, y_j), j \in [1, m]\}$ is a set of data points of length m, and t is an independent variable,
$f(t, p)$ is a model function with a vector parameter p of size n,
σ_{y_j} is a parameter related to the weighting matrix W whose diagonal is equal to $W_{jj} = \frac{1}{\sigma^2_{y_j}}$,
$J = \frac{\partial y}{\partial p}$ is a $m \times n$ Jacobian matrix representing the variation of the data points in terms of the modal parameter p and J^T is its transpose,
I is an identity matrix, and ϑ is a determinant parameter.

If the determinant parameter, ϑ, is small, we get a Gauss-Newton update where it is assumed that the objective function χ^2 is approximately quadratic in the parameters and the parameters values are close to their optimal values. A large value of ϑ results to a Gradient descent update function where the parameters are far from their optimal values. Updating the modal parameters is executed in the opposite direction of the gradient of the objective function. Details of this technique have been developed elsewhere [25].

Stellenbosch University https://scholar.sun.ac.za

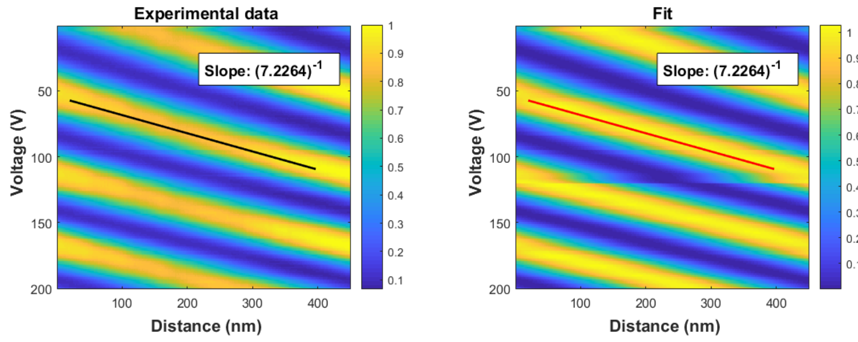

Figure 3.5: *Interference intensity profile as a function of the applied voltage on the piezoelectric. Left: Experimental data. Right: Fitted data. The slope of the two lines (black and red) is approximately equal to* 7.23^{-1} *V/nm.*

$0) - y_V(x = 0, \delta)|$ is minimum, where $y(x = 0)$ is the experimental intensity value at position $x = 0$, y_V is the function defined in Equation (3.3.3) and evaluated at $x = 0$ for different values of δ in range of 0 to 2π.

The optical path length difference of the light that reflects off from D1 and D2 is double the physical distance between the two mirrors. The calibration factor of the piezoelectric can therefore be deduced from the half of the inverse of the slope of a line, made up from data points with approximately same intensity in Figure 3.5, which is approximately equal to 3.62 nm/V, or using the interference shift parameter δ (Figure 3.6).

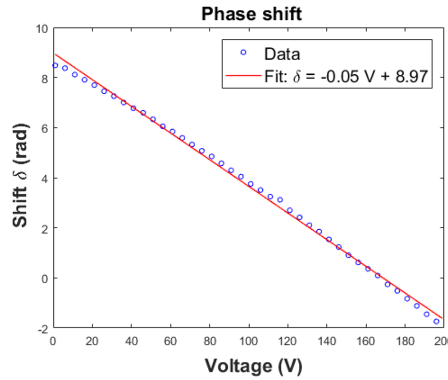

Figure 3.6: *Phase shifting parameter as a function of the applied voltage.*

A phase shift equal to $\Delta\delta = 2\pi$ corresponds to a wave traveled distance equal to the wavelength 854.3 nm and a voltage ΔV = 117.44 volts (using the equation on Figure 3.6). That yields to a conversion factor equal to 7.27 nm/V. The axial calibration factor is therefore equal to 3.64 nm/V using the interference shift parameter.

Stellenbosch University https://scholar.sun.ac.za

Chapter 4

Localization analysis

The position of an emitter over time can vary either in a predictable fashion or randomly, therefore localization analysis of the emitter's position may be approached through appropriate statistical models. There are many factors limiting the localization of a single emitter such as the optical system itself and the emission properties of the emitter. In this chapter, those factors are developed, the experimentally obtained single emitter images are analyzed to determine the lateral and axial positions, and a theoretical study of a bisected and a pyramidal engineered PSFs are compared with the DH-PSF in order to reveal the depth information and the orientation of an isotropic and a dipole emitter.

4.1 Statistical models

A key goal of the wide-field fluorescence microscopy technique developed for this work is to achieve a very high localization precision and accuracy in order to get precise information about the emitter's position in three dimensional space. When tracking an isotropic emitter, such as a spherical nanoparticle, or a radiating dipole, such as a single fluorescent molecule, the localization precision and accuracy are very important.

Let us define the true position of a single particle p by (x_p, y_p). This true position is experimentally unknown. The set of the estimates positions of the particle p over a given number of frame images, n, is denoted by $\{(x_{p|i}, y_{p|i}),\ i \in [1, n]\}$. The position (x, y) here is defined in terms of pixel position in an image. By definition, the localization precision is a measure of the deviation of each estimate position, $(x_{p|i}, y_{p|i})$, around the average of the estimate positions, $(\overline{x}_p, \overline{y}_p)$, while the localization accuracy is the measure of the deviation of the average of the estimate positions, $(\overline{x}_p, \overline{y}_p)$, around the true position, (x_p, y_p) [26]. Since (x_p, y_p) is experimentally unknown, and is needed to be estimated, the localization accuracy can be defined in terms of the number of occurrences of the deviation $(\Delta x_i, \Delta y_i) = (x_{p|i} - \overline{x}_p, y_{p|i} - \overline{y}_p)$.

Stellenbosch University https://scholar.sun.ac.za

The location of a particle can be estimated using the center of mass technique or by fitting the intensity distribution of the image by means of a model, such as the Airy pattern (PSF) as the smallest object, which is a point source, that can be imaged appears like an Airy pattern (Section 2.3.3). The center of mass technique consists of finding the intensity-weighted mean of the x and y coordinates in a given region of interest. This technique is computationally fast but not precise and accurate enough in presence of noise in the images. Also, information that can be extracted from a set of data from a center of mass technique, such as the emitter size, are very limited [27]. In our case, we consider the second approach; the use of a model to fit the intensity distribution to obtain the location of a particle.

4.2 Localization limits

When an emitter emits a given number of photons N_0, a portion N_0' of N_0 is collected by the camera as detector within an exposure time t, and converted into a digital image. Let $N(t)$ denote the number of converted photons, which is less than the collected photons N_0', due to the efficiency of the camera and the exposure time. An image is characterized by the number of photons $N(t)$ collected and converted within a given exposure time t, $t > 0$. The photon number is influenced by factors such as the efficiency of the system and detector, the exposure time of the detector, and some noise and vibration sources due to the environment where the measurement is conducted [28].

Matching the emission pattern over an adequate number of pixels is also very important. If the magnification of the system is low, the pattern is distributed over a few pixels. This decreases information about the emission pattern [28]. If the magnification is too large, some information might be lost, because the finite size of the pixels implies that the emission pattern will spread over a large number of pixels thus decreasing the signal strength. [28]. Due to these factors, the precision and accuracy for a localization are limited. Therefore, it is beneficial to know what is the smallest achievable error for a particular measurement. As error in a given measurement corresponds to the precision of the localization.

The smallest achievable localization precision has been derived in many text-books and journal papers [10, 26, 28, 29] using the Fischer information matrix. The Fischer information matrix is the measure of information about a vector parameter (x, y) in observed data $\{(x_{p|i}, y_{p|i}),\ i \in [1, n]\}$ where n is the number of estimate positions, which also corresponds to the number of frames when a stack of images are recorded. Higher Fischer information about one parameter means higher precision for measuring that parameter. The Fischer information matrix in two dimensional space, within an assumption that the existing noise

Stellenbosch University https://scholar.sun.ac.za

follow a Poisson distribution, is given by the following expression [29]

$$\begin{aligned} I(x,y) &= \begin{pmatrix} I_{11} & I_{12} \\ I_{21} & I_{22} \end{pmatrix} \\ &= \gamma E[N_0'] \int_{\mathbb{R}^2} \frac{1}{q(x,y)} \left[\frac{\partial q(x,y)}{\partial x}, \frac{\partial q(x,y)}{\partial y} \right]^T \left[\frac{\partial q(x,y)}{\partial x}, \frac{\partial q(x,y)}{\partial y} \right] dx\ dy, \end{aligned} \tag{4.2.1}$$

where the exponent T indicates the transpose operator, γ is the efficiency of the detector system, $E[N_0']$ denotes the average value of the collected photons N_0', which is equivalent to the emission rate of the emitter multiplied by the exposure time t of the detector, and therefore $\gamma E[N_0']$ corresponds to the photon number $N(t)$.

If the image function q is symmetric, *i.e.* $q(-x,y) = q(x,-y)$, then $I_{12} = I_{21} = 0$, but $I_{11} = I_{22}$ is not necessarily true. The limit of the localization precision is given by the inverse of the square root to the Fischer information matrix, defined as the Cramer-Rao Lower Bound (CRLB) [30].

Consider the standard Airy PSF image distribution approximated by an appropriate Bessel function, the image function is defined as

$$q(x,y) = \frac{\mathcal{J}_1^2(\alpha(x^2+y^2)^{1/2})}{\pi(x^2+y^2)}, \tag{4.2.2}$$

where $\mathcal{J}_1$ is the Bessel function first kind, $(x,y) \in \mathbb{R}^2$, and $\alpha = \frac{2\pi \text{NA}}{\lambda_{\text{emission}}}$, with NA: numerical aperture of the microscope objective in the imaging setup, and $\lambda_{\text{emission}}$: emission wavelength [28]. Equation (4.2.2) is symmetric and the Fischer information is given by

$$I(x,y) = N(t) \left(\frac{2\pi \text{NA}}{\lambda_{\text{emission}}} \right)^2 \begin{pmatrix} 1 & 0 \\ 0 & 1 \end{pmatrix}. \tag{4.2.3}$$

Using the CRLB, the limit of the localization precision for a standard PSF image function is given by

$$\delta_x = \delta_y = \frac{\lambda_{\text{emission}}}{2\pi \text{NA} \sqrt{N(t)}}. \tag{4.2.4}$$

This result suggests that the localization precision in both x and y directions are improved when choosing a large numerical aperture microscope objective and very bright emitters (large $N(t)$). Also the smaller the emission wavelength the better for localization, however this is not always practically possible.

Furthermore, this PSF has several secondary maximas (intensity rings on a 2D image). Experimentally speaking, the intensity at the center of a PSF is dense, and its rings may become unclear due to background noise in a

Stellenbosch University https://scholar.sun.ac.za

measurement [28]. An alternative solution for quantifying the localization precision consists of using a Gaussian function for fitting the intensity distribution of the emitter. The Gaussian image function is given by

$$q(x,y) = \frac{1}{2\pi w_g^2}\, e^{-\frac{x^2+y^2}{2w_g^2}}, \tag{4.2.5}$$

where w_g is the standard deviation of the distribution [30]. The function q is symmetric and the Fischer information in x and y directions are equal [30].

$$\begin{aligned} I_{11} = I_{22} &= \gamma E[N_0'] \int_{\mathbb{R}}^{2} \frac{1}{q(x,y)} \left[\frac{\partial q(x,y)}{\partial x}\right]^2 \, dx\; dy \\ &= \frac{N(t)}{w_g^2}. \end{aligned} \tag{4.2.6}$$

Hence, the limit of the localization precision, defined by the CRLB, is

$$\delta_x = \delta_y = \frac{w_g}{\sqrt{N(t)}}. \tag{4.2.7}$$

As the Gaussian distribution is narrower, its standard deviation w_g is smaller, and the limit of the localization precision is smaller. In both cases, using a PSF model or a Gaussian model, the limit of the localization precision is inversely proportional to the square root of the photon number $N(t)$.

Generally, the localization precision of an emitter p over a given number of images n can be defined in terms of the following standard deviation:

$$\sigma_x = \sqrt{\frac{1}{n-1}\sum_{i=1}^{n}(x_{p|i} - \overline{x}_p)^2}. \tag{4.2.8}$$

As the number of measurements, defined by the number of recorded images, n, is larger, the parameter σ_x is smaller and tends to the limit δ_x defined in Equation (4.2.7).

On the other hand, the localization precision can also be determined differently. The number of occurrences m, of the deviation $\Delta x_i = x_{p|i} - \overline{x}_p,\; i \in [1,n]$ [26], follows a Normal distribution centered at 0, and with a standard deviation σ_x, for a large n. Here a large σ_x implies that, the number of estimate positions which are far from the mean position is also large, hence the localization is not precise, but not necessarily inaccurate.

The same principle can be applied to the position of the particle along the y direction, and the theory can be generalized for a $3-$D spatial coordinates (x,y,z).

Stellenbosch University https://scholar.sun.ac.za

In the next section, the lateral positions of three different NPs with different sizes (600 nm, 300 nm, and 50 nm) are analyzed. The corresponding localization precision and accuracies are compared with the limit of the localization precision defined by the CRLB. The three NPs are assumed to be spherical and that the emission is isotropic.

4.3 Lateral localization precision and accuracy

Three isolated NPs with different sizes; polymer based NPs with size of about 600 nm, polymer based NPs with size in range of 300 nm and 400 nm, and 50 nm fluorescent silica nanobeads, are embedded in a polystyrene media, and are imaged with the setup described in Section 3.2. The NPs radiate in both channels: horizontal and vertical (Figure 4.1). As described in the schematic diagram of the experimental setup 3.2, the light from the emitter is split into horizontal and vertical polarized orientations using a polarizing beam splitter (PBS). The horizontal light is transmitted and reflected horizontally on the screen of the SLM by two prisms whereas the vertically polarized light is reflected by the PBS, first flipped by one prism, then rotated horizontally by 90° by another prism. The light from the two paths exit the system {PBS + 4 prisms} parallely, and arrive horizontally on the SLM. The SLM's inclination is adjusted in such a way that the light from the two paths fit on the SLM's screen, and with the same path length. Images of the fluorescence emission are recorded with the sCMOS digital camera.

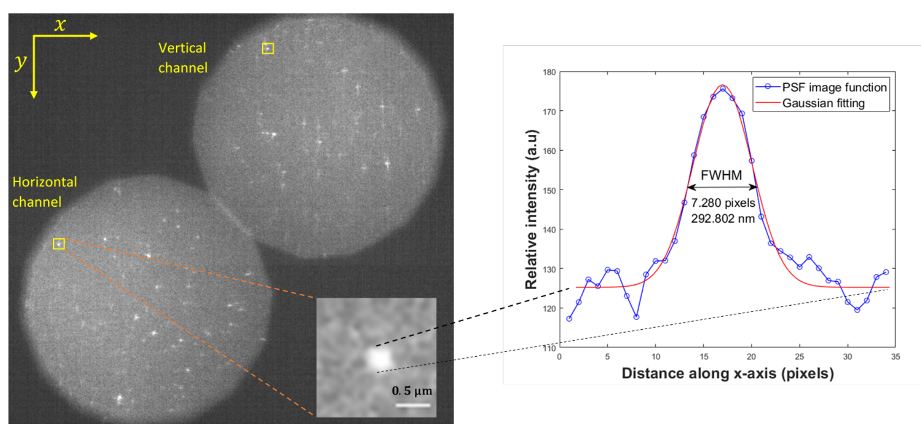

Figure 4.1: *Single nanoparticle emission. Left: Image of the horizontal polarization and vertical polarization channels. Right: Intensity profile along the x axis of one emitter, plus a Gaussian fit with FWHM of* 292 *nm.*

To evaluate the localization of the isolated NPs, a sample containing the NPs, a stack of images is recorded within a pre-defined exposure time of the camera. As discussed in the previous section, the localization is more precise if the

Stellenbosch University https://scholar.sun.ac.za

number of acquisitions or/and the number of collected photons are large. A large photon number can be obtained by increasing the exposure time. However, a long exposure time permits a higher probability of photodamage that leads to a quick destruction of the localization precision and accuracy. A balance between the exposure time, the photobleaching rate of the NP, and the sampling size, which corresponds to the number of images to record, must then be taken into account. Accordingly, the acquisition time is set to be 500 ms for all the measurements conducted in our experimentation. The number of recorded images, which defines the number of the estimate positions of the emitter, is chosen in function of the size of the NP. The 600 nm polymer based NPs are imaged in a stack of 100 images. Whilst 50 images for the 300 nm polymer based NPs, and 30 images are recorded for the fluorescent silica 50 nm nanobeads.

Image processing is required before conducting any imaging analysis so as to increase the signal-to-noise ratio, which improves the precision and accuracy of any localization [28]. The process of image processing is carried out using free software, called ImageJ (imagej.net). A region of interest (ROI) containing the image of one emitter is selected. Another region with the same size as the ROI is selected, either on the horizontal channel region or on the vertical channel, which contains only background noise. The background noise is subtracted from the ROI containing the image of an emitter. The background free image is ready to be analyzed after minor additional filtering. There are several techniques for filtering an image in fluorescence microscopy. The nonlinear smoother LULU operator, described in [27], is a good filter for fluorescence imaging. The ImageJ software also possesses different kind of built-in function filters such as the Gaussian blur filter, median filter or maximum and minimum filter.

In Figure 4.1(Right), the intensity profile of a single fluorescent NP along the x-axis is fitted with a Gaussian function. This fit is a line-out of the two dimensional fit procedure employed for this work. The two dimensional Gaussian function for the least squares fit procedure is given as follows

$$G(x, y) = A\ e^{-\frac{(x-x_{p|i})^2+(y-y_{p|i})^2}{2w_g^2}} + B, \tag{4.3.1}$$

where A is the amplitude of the Gaussian function, B is an offset, w_g is the width, and $(x_{p|i}, y_{p|i})$ corresponds to the estimate position of the nanoparticle emitter p at a given image frame i, whose initial guess can be extracted by finding the center of mass position of the selected ROI in image i. The Gaussian fitting is done using a non-linear least square technique [27]. The full width half maximum (FWHM) of the Gaussian function may be used to estimate the size of the emitter (provided that the expected width is greater than the

Stellenbosch University https://scholar.sun.ac.za

diffraction limit), and is given by

$$\text{Size(NP)} = 2\sqrt{2\log 2}\, w_g\, C, \tag{4.3.2}$$

where C is the conversion factor of the system, and calculated be equal to 40.22 nm/pixel in Section 3.2.2.

Furthermore, the limit of the localization precision for a particular measurement can be derived using Equation (4.2.7). It is proportional to the width w_g, of the Gaussian function, and inversely proportional to the square root of the number of photons $N(t)$. A large width w_g corresponds to a bigger limit of the localization precision. The number of photons on the other hand is determined using a simple conversion formula provided with the camera

$$N(t) = \frac{CF\ (PIX - Off)}{Q(\lambda)/100}, \tag{4.3.3}$$

where CF is the conversion factor, and equal to 0.47 electrons/count, PIX is the intensity pixels of interest, which is known from the emitter's image, Off is an offset value, and equal to 110 for our system, and $Q(\lambda)$ is the quantum efficiency of the detector which is equal to 81% for the corresponding emission wavelength 550 nm.

Note that a precise localization is not necessarily accurate, and vice versa. As such, apart from determining the localization precision, one also need to evaluate the localization accuracy. As already mentioned in the above section, the localization accuracy may be defined in terms of the number of occurrences of the deviation, $(\Delta x_i, \Delta y_i) = (x_{p|i} - \overline{x}_p, y_{p|i} - \overline{y}_p)$. This number of occurrences can be considered as a random variable; knowing the distribution of this variable allows us to derive its probability density function, thus enables the determination of the localization accuracy. A distribution with a mean equal to or close to 0, concentrated at the 0 mean, and symmetric about the 0 mean is equivalent to a more accurate system.

The probability distribution of the deviation of the estimate positions from the mean for each of the three isolated nanoparticles is plotted in Figure 4.2. As can be seen in this figure, the deviation of the estimate positions from the mean for each case follows a normal distribution. The underlying mean is thus equal to 0. The localization of the 300 nm nanoparticle is less accurate than the localization of the 600 nm and 50 nm nanoparticles, where one can say that a more desirable localization accuracy is achieved.

From the Table 4.1, the physical size of the silica nanoparticle is calculated to be bigger than 50 nm. This is due to the fundamental diffraction limit described by the Rayleigh criterion[1].

[1] The Rayleigh criterion defines the minimal resolved distance d between two objects or

Stellenbosch University https://scholar.sun.ac.za

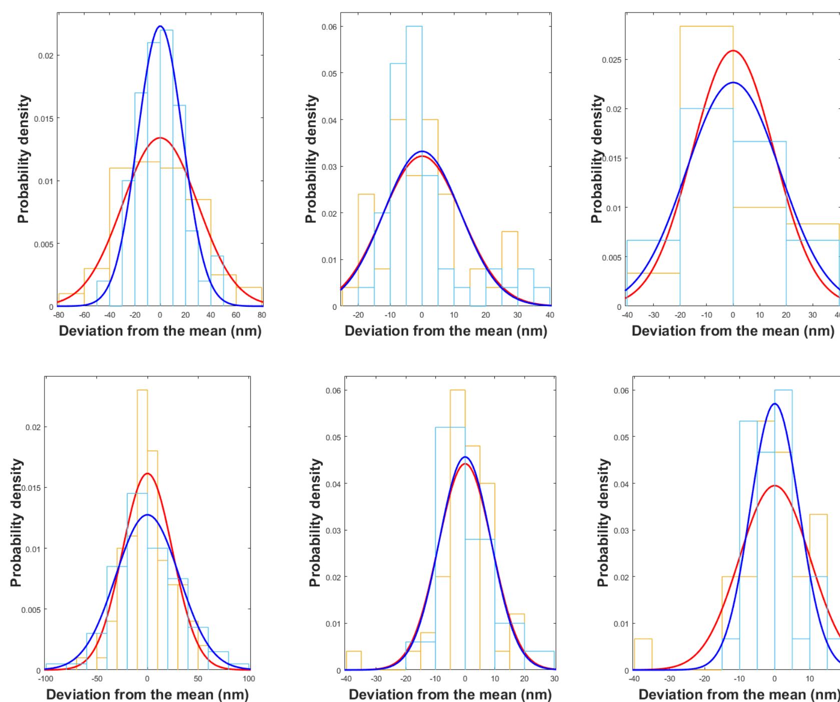

Figure 4.2: *Localization accuracy of nanoparticle emitters. The first row corresponds to the data collected from the horizontal channel while the second row corresponds to the vertical channel. The first, second, and third columns are associated to the distribution (colored red for localization along the x-axis and blue for localization along the y-axis) of the deviation of the estimate positions from the mean for* 600 *nm,* 300 *nm, and* 50 *nm nanoparticles respectively. The probability that a deviation with respect to a particular range Δx (Δy respectively) will happen is determined by the underlying area defined under the probability density function (block diagram orange for localization along x-axis and cyan along the y-axis).*

The limit of the localization precision in the three cases are different for horizontal and vertical channel even though the width of the image Gaussian function w_g is the same for both channels for the silica NP. This means, the amount of light in both channels are not identical. Furthermore, due to the slight offset angle in the placement of the SLM in the experimental setup, the imaging of the two channels are not the same.

The localization precision (error) obtained for the 3 objects compares well with literature [31] where Grover et. al. managed to locate a bright fluorescent

minimal resolved object size [11]:

$$d = 0.61 \, \frac{\lambda_{\text{emission}}}{\text{NA}},$$

where $\lambda_{\text{emission}}$ is the wavelength emission and is equal to 550 nm in our case, and NA is 1.3. A distance or object size smaller than d will be imaged slightly bigger or within the same size as d.

Stellenbosch University https://scholar.sun.ac.za

Table 4.1: *Results for lateral localization analysis. $\overline{N}$ and LLP denote the average photon number over a first five measurements with a standard error σ_N and the limit of the localization precision respectively.*

	600 nm (100 images)		300 - 400 nm (50 images)		50 nm (30 images)	
	H	V	H	V	H	V
$\overline{\mathrm{N}}$	33366	39196	6125	7253	7387	7820
σ_{N}	876	869	338	399	199	407
$\overline{w}_g$ (pixels)	7.51	9.39	3.61	3.45	3.24	3.24
σ_{w_g}	0.35	1.33	0.24	0.25	1.00×10^{-4}	1.00×10^{-4}
LLP $\delta_x = \delta_y$	1.65	1.91	1.86	1.63	1.52	1.47
Size (nm)	711	889	342	327	307	307
σ_x (nm)	30	25	12	9	15	10
σ_y (nm)	18	31	12	9	18	7

molecule (N= 6985 ± 1390) with lateral errors of $(\sigma_x, \sigma_y) = (18\text{nm}, 30\text{nm})$.

Furthermore, the localization precision in the horizontal and vertical channels differs. This is a consequence of slight astigmatism in the optical system. The astigmatism can be corrected by displaying an appropriate phase mask on the SLM. However, this is beyond the scope of the work [20].

4.4 Experimental results for axial position using DH-PSF engineering

The third dimension, indicating the location of an emitter along the optical axis, can be accessed by modulating the phase of the light in such a way that the intensity pattern at the image plane is sensitive to the axial position. Several techniques have been developed to achieve the axial localization of an emitter. The DH-PSF has been proved to surpass many techniques in achieving a better localization precision over 2 μm range [32]. Correspondingly, this section shows and discusses the experimental results for DH-PSF phase modulation.

Depth information via the axial position

The sample used for testing the ability of the DH-PSF modality consist of the 600 nm polymer based NPs embedded in a thin polystyrene film. This choice

Stellenbosch University https://scholar.sun.ac.za

is based on its high photon emission rate compared to the other NP samples. Stated in the experimental setup, the piezoelectric stage is connected to the microscope objective. Therefore when a voltage is applied to it, the objective moves up or down changing the relative axial position between the stationary emitter and the focal plane. This defocusing and focusing by translating the objective has the same effect at the image plane (on the camera) as moving the emitter instead of the objective. Thus, it is thought of that the emitter's axial position is controlled by the piezoelectric stage by an amount d either up or down along the $z-$axis. The applied voltage is increased in steps of 20 V and 3 images are taken per step. In total, 14 voltage steps were recorded, five of which are shown in Figure 4.3. Using the calibration factor of the piezo in Section 3.3, we can say that an increase of applied voltage equal to 20 V corresponds to a displacement of 0.145 ± 0.028 μm in z.

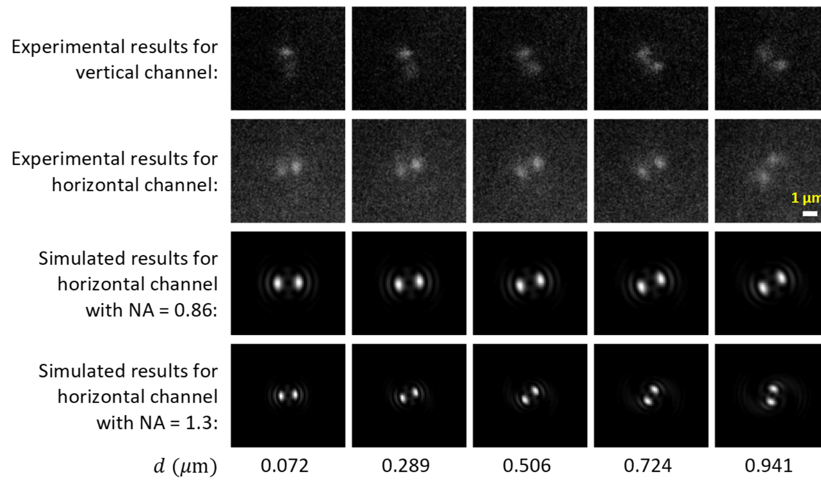

Figure 4.3: *Image comparatives of the DH-PSF from experimental results and simulated DH-PSFs of an isotropic emitter with NA = 0.86 and NA = 1.3 for different defocus distances d. The simulated results rotate more than the experimental results due to the NA used for the simulation. The NA has been reduced experimentally by closing the iris on the pathway.*

From Figure 4.3, it is clear that as the distance of defocus increases, the two lobes rotate around the axial axis. The angle between a horizontal line and the line passing by the two lobes is thus a function of d which corresponds to a specific axial position z (Figure 4.4). In order to find the rotation angle of the two lobes about a horizontal line, the intensity pattern of the two lobes is fitted in a non-linear least square fitting by a double Gaussian (DG) function given by

$$\mathrm{DG}(x, y) = A_1 \exp[-\tfrac{(x-x_1)^2+(y-y_1)^2}{2w_1^2}] + A_2 \exp[-\tfrac{(x-x_2)^2+(y-y_2)^2}{2w_2^2}], \quad (4.4.1)$$

Stellenbosch University https://scholar.sun.ac.za

where A_i, w_i, and (x_i, y_i) are the amplitude, width, and centroid of the lobe $i, i \in [1, 2]$ respectively. The lateral position (x_c, y_c) of the emitter is given by the mean of the two lobe centroids. Therefore, the 3 points, $\{(x_1, y_1), (x_c, y_c), (x_2, y_2)\}$, form the required line for determining the rotation angle of the two lobes. The experimental results are plotted in Figure 4.4.

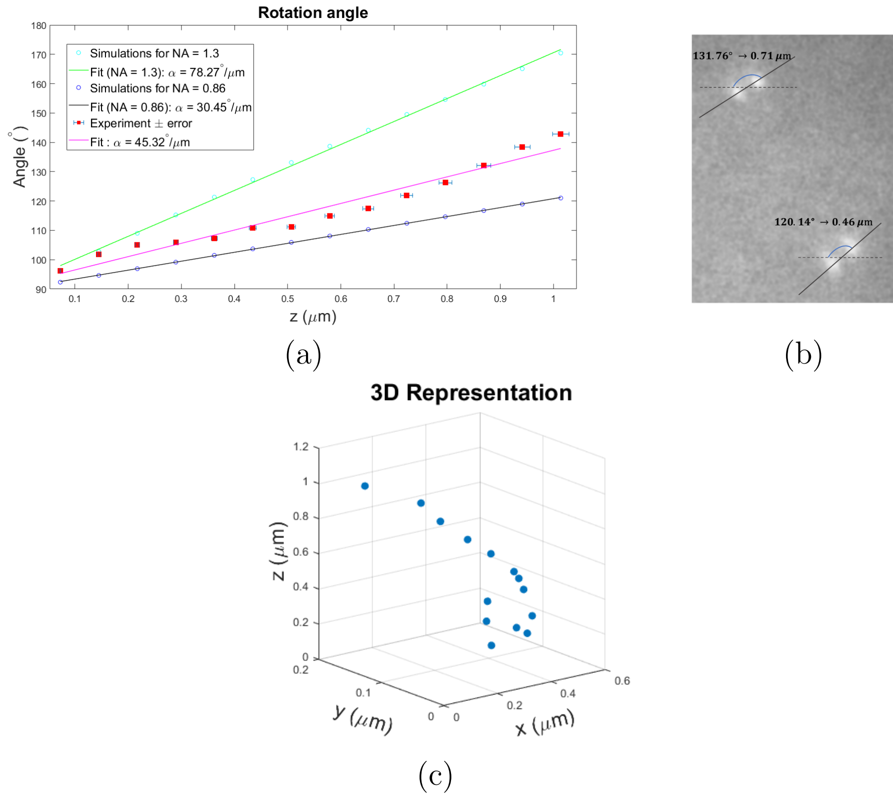

(a) (b)

(c)

Figure 4.4: *The angle of the rotation line of the two lobes changes monotonically as a function of the z position. (a) Angle between the horizontal line and the line of the two lobes with respect to the z position. (b) Fluorescence emission of two emitters with different defocus distances. (c) 3D estimate positions of one emitter.*

The rotation rate α of the experimental data has been shown smaller than the rotation rate of the simulated data with the NA of the microscope objective which is equal to 1.3 ($45.32°/\mu$m against $78.27°/\mu$m). This difference is attributed to the smaller effective numerical aperture of the optical system, as is evident in Figure 4.4(a) where a comparable simulated rotation rate is achieved using a NA between 0.86 and 1.3. The numerical aperture and hence the field of view on the image plane is decreased using an iris (Figure 3.2) in order for the polarized beams (transmitted and reflected) to fit on the screen on the SLM. Interestingly this implies that the rotation rate can be increased or decreased by playing with the size of the diameter of the iris. Therefore, if precise information about the axial position in a small range of z is required,

Stellenbosch University https://scholar.sun.ac.za

one need only increase the NA by increasing the diameter of the iris. However if deep imaging is important, a lower rotation rate (small NA, small iris diameter) is chosen.

Additionally, the defocus distances, hence axial positions z, of different emitters can be determined simultaneously (Figure 4.4(b)), and the estimate positions of one emitter in 3D is shown in Figure 4.4(c). The localization precision (error) of the axial position is equal to $\sigma_z = 31$ nm in the horizontal channel and 30 nm in the vertical channel. On the other hand, the localization precision in the lateral position is $(\sigma_x, \sigma_y) = (92\,\text{nm}, 45\,\text{nm})$ and $(\sigma_x, \sigma_y) = (66\,\text{nm}, 107\,\text{nm})$ in the horizontal and vertical channels respectively. These results can be improved by increasing the sampling size. Care also must be taken when determining the lateral position of an emitter in such a fashion, because if the emission is anisotropic, erroneous localization can result in severe mislocalization [33].

The next section gives an overview of how one can find the orientation of an emitter using DH-PSF and compared to other PSF phase masks.

4.5 Simulated results of the orientation of a dipole emitter

In the previous section DH-PSF engineering is used to determine the axial position of an emitter. However, from the theoretical studies in Section 2.3.4 and specifically the simulated results in Figure 2.19, it was clear that the imaged emission of a single dipole is sensitive to its orientation as the two lobes had different intensities. This section focuses on the differences of the lobe intensities and how it depends on the orientation of a single dipole emitter.

Determination of the orientation of a dipole emitter

The orientation of a dipole emitter can be determined using (a look-up table of) the linear dichroism (LD) and the lobe asymmetry (LA) of the double lobes in each channel horizontal and vertical. These two parameters are defined as follows

$$\text{LD} = \frac{N_H - N_V}{N_H + N_V} \quad \text{and} \quad \text{LA}_{H,R} = \frac{A_{H,R|1} - A_{H,R|2}}{A_{H,R|1} + A_{H,R|2}}, \tag{4.5.1}$$

where N_H, N_V are the total number of photons in the horizontal (transmitted light) and vertical channels (reflected light) respectively, and $A_{H,R|1}$ and $A_{H,R|2}$ are the amplitudes of lobe 1 and lobe 2 in each channel horizontal (H) and vertical (V) [23]. Here the amplitudes are determined using a two-dimensional double Gaussian fit function.

Stellenbosch University https://scholar.sun.ac.za

Simulations of a dipole emitter with different orientation and imaged around the focal plane using DH-PSF engineering is computed. The LD and LA values are determined and plotted in Figure 4.5. The results in Figure 4.5 can be used as a look-up table for pattern matching to deduce the orientation of the emitter, because each orientation gives unique LA and LD values for a given axial position.

Accurate and precise pattern matching consists of finding the orientation for different defocus distances. Care must however be taken as the LA changes drastically for a given orientation under varying defocus values.

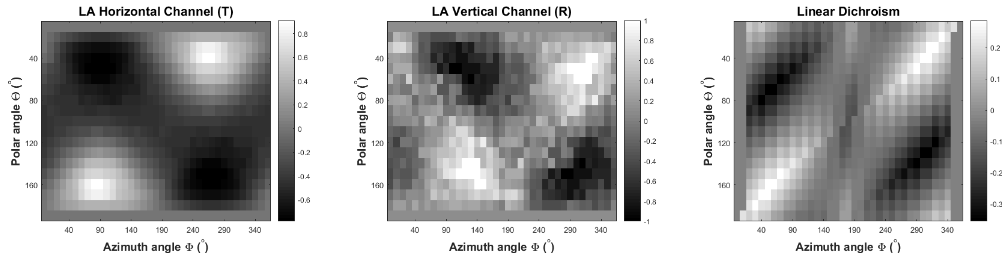

Figure 4.5: *Lobe asymmetry of the two lobes in horizontal channel and vertical channel, and linear dichroism at the focal plane with defocus distance* 0.

Alternative PSFs can also be useful for finding the axial position, lateral position, and orientation of an emitter: bisected and pyramidal PSFs.

Bisected and pyramidal PSFs

The phase masks for generating a bisected PSF and a pyramidal PSF are plotted in Figure 4.6. A bisected phase mask is given by the equation

$$\phi_{\text{Bisected}} = C_0 - \frac{C_0}{\sin\theta_{\text{max}}}|y|, \tag{4.5.2}$$

where θ_{max} is the maximal aperture of the field of view derived from the expression of the NA, and C_0 is the maximum phase whose the minimal effective value associated with NA $= 1.3$ is equal to 3π. The constant C_0 can be tuned to control the slope and magnitude of the phase. On the other hand, the pyramidal phase mask is given by

$$\phi_{\text{Pyramidal}} = C_0 - \frac{C_0}{\sin\theta_{\text{max}}}(|x| + |y|), \tag{4.5.3}$$

where the effective minimal value of C_0 corresponds to 6π [23].
The results on the phase modulation of an isotropic and a dipole emitter, with emission wavelength 550 nm, are plotted in Figure 4.7. The bisected PSF consists of two lobes whose interlobe distance is a function of the defocus

Stellenbosch University https://scholar.sun.ac.za

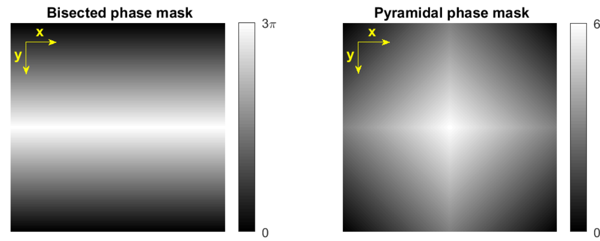

Figure 4.6: *Phase masks for bisected and pyramidal PSFs.*

distance whereas the pyramidal PSF is formed of four lobes expanding with increase of distance d. The asymmetry on the two PSFs for d positive and d negative make them extremely useful in a number of fluorescence microscopy techniques [23].

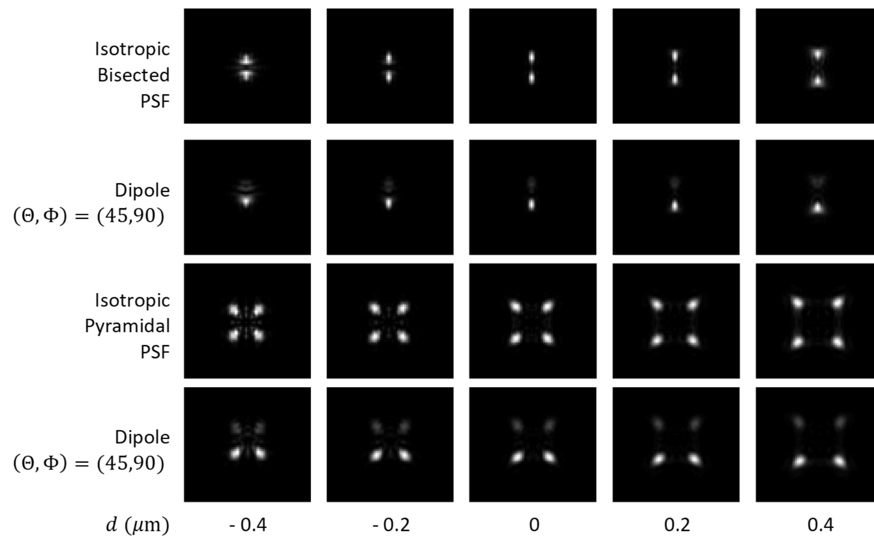

Figure 4.7: *Bisected and pyramidal PSF of an isotropic and a dipole emitter at different defocus distance d. The intensity of each lobe of the PSF is function of the orientation of the emitter whereas the distance between each lobes determines its defocus distance.*

Experimentally, a bisected PSF is more advisable for finding the axial position, because pyramidal PSF requires a high emitted photon number as the light is split into eight spots in the horizontal and vertical channels. However, the pyramidal PSF, also called quadrated PSF, is more efficient for finding the orientation of an emitter [23].

Stellenbosch University https://scholar.sun.ac.za

Chapter 5

Conclusion

In conclusion, a phase modulation of fluorescence emission is modeled computationally through this project in order to achieve a double helix point spread function (DH-PSF) imaging. The main goal of the work consists of locating a fluorescent emitter in three dimensional space with a high accuracy and precision, and to find its orientation. A particular model with experimental parameters (wavelength emission $\lambda = 550$ nm, numerical aperture NA $= 1.3$, refractive index of 1.5) is chosen as a reference for further experimental validation of the work. Experimentally, a $4f$-type imaging system is implemented to image fluorescent emitter objects, which consist of 50 nm diameter fluorescent silica nanoparticles, 300 nm and 600 nm polymer based nanoparticles embedded in polystyrene media. The phase modulation is achieved using a spatial light modulator (SLM) device.

Many factors limiting the measurement are discussed and the limit of the localization precision, defined using the Fischer information matrix, is shown experimentally to be less than 2 nm in three directions (x, y, z). The lateral position is found with a high accuracy and precision in the order of $10 - 30$ nm. Furthermore, the DH-PSF engineering has been proved experimentally to be able to retrieve simultaneously the axial and the lateral position of the emitter. The localization errors using the DH-PSF imaging seem bigger and are in order of 0.1 μm, but can still be improved by correcting the aberrations and distoritions in the system using the SLM. However, the errors are still small compared to the size of the emitter object (~ 0.6 μm). In addition, the DH-PSF imaging has also been shown to be able to give information about the orientation of an anisotropic emitter such a dipole.

Lastly, this work can be generalized for studying single molecule diffusion in three dimensional space. Experimental comparisons of the efficiency of the three PSFs: bisected PSF, pyramidal PSF, and the DH-PSF or/and a new engineered PSF are envisaged for the future in order to achieve a high resolution fluorescence microscopy.

Stellenbosch University https://scholar.sun.ac.za

List of References

[1] Sri Rama Prasanna Pavani, Jennifer G DeLuca, and Rafael Piestun. Polarization sensitive, three-dimensional, single-molecule imaging of cells with a double-helix system. *Optics express*, 17(22):19644–19655, 2009.

[2] Sabine Daemen, Marc AMJ van Zandvoort, Sapun H Parekh, and Matthijs KC Hesselink. Microscopy tools for the investigation of intracellular lipid storage and dynamics. *Molecular metabolism*, 5(3):153–163, 2016.

[3] Otto S Wolfbeis. An overview of nanoparticles commonly used in fluorescent bioimaging. *Chemical Society Reviews*, 44(14):4743–4768, 2015.

[4] Ulrich Kubitscheck. *Fluorescence microscopy: from principles to biological applications*. John Wiley & Sons, 2013.

[5] Isabel Rodrigues and João Sanches. Photoblinking/photobleaching differential equation model for intensity decay of fluorescence microscopy images. In *Biomedical Imaging: From Nano to Macro, 2010 IEEE International Symposium on*, pages 1265–1268. IEEE, 2010.

[6] Philip Tinnefeld, Christian Eggeling, and Stefan W Hell. *Far-Field Optical Nanoscopy*, volume 14. Springer, 2015.

[7] Michael J Sanderson, Ian Smith, Ian Parker, and Martin D Bootman. Fluorescence microscopy. *Cold Spring Harbor Protocols*, 2014(10):pdb–top071795, 2014.

[8] J David Jackson. *Electrodynamics*. Wiley Online Library, 1975.

[9] David J Griffiths. *Introduction to electrodynamics*. Prentice Hall, 1962.

[10] Lukas Novotny and Bert Hecht. *Principles of Nano-Optics*. Cambridge University Press, New York, 2006 edition.

[11] Eugene Hecht and A Zajac. Optics. 3rd. *Edn., Addison-Wesley, Reading, MA*, 1997.

[12] C Farina and W. J. M. Kort-Kamp. On the exact electric and magnetic fields of an electric dipole. *American Journal of Physics 79*, 111, 2011.

[13] Joseph W Goodman. *Introduction to Fourier optics*. Roberts and Company Publishers, 2005.

Stellenbosch University https://scholar.sun.ac.za

[14] Okan K Ersoy. *Diffraction, Fourier optics and imaging*, volume 30. John Wiley & Sons, 2006.

[15] Carmelo Rosales-Guzmán and Andrew Forbes. How to shape light with spatial light modulators. In *SPIE. SPOTLIGHT*, 2017.

[16] Jerneja Pavlin, Nataša Vaupotič, and Mojca Čepič. Liquid crystals: a new topic in physics for undergraduates. *European Journal of Physics*, 34(3):745, 2013.

[17] Grigory Lazarev, Andreas Hermerschmidt, Sven Krüger, and Stefan Osten. Lcos spatial light modulators: trends and applications. *Optical Imaging and Metrology: Advanced Technologies*, pages 1–29, 2012.

[18] Holoeye. Spatial Light Modulators User's guide, 2013.

[19] Clemens Roider, Alexander Jesacher, Stefan Bernet, and Monika Ritsch-Marte. Axial super-localisation using rotating point spread functions shaped by polarisation-dependent phase modulation. *Optics express*, 22(4):4029–4037, 2014.

[20] Bo Huang, Wenqin Wang, Mark Bates, and Xiaowei Zhuang. Three-dimensional super-resolution imaging by stochastic optical reconstruction microscopy. *Science*, 319(5864):810–813, 2008.

[21] Matthew D Lew, Steven F Lee, Majid Badieirostami, and WE Moerner. Corkscrew point spread function for far-field three-dimensional nanoscale localization of pointlike objects. *Optics letters*, 36(2):202–204, 2011.

[22] Yoav Shechtman, Lucien E Weiss, Adam S Backer, Steffen J Sahl, and WE Moerner. Precise three-dimensional scan-free multiple-particle tracking over large axial ranges with tetrapod point spread functions. *Nano letters*, 15(6):4194–4199, 2015.

[23] Adam S Backer and WE Moerner. Extending single-molecule microscopy using optical fourier processing. *The Journal of Physical Chemistry B*, 118(28):8313–8329, 2014.

[24] N Sultanova, S Kasarova, and I Nikolov. Dispersion proper ties of optical polymers. *Acta Physica Polonica-Series A General Physics*, 116(4):585, 2009.

[25] Henri Gavin. The levenberg-marquardt method for nonlinear least squares curve- fitting problems, 2011.

[26] Hendrik Deschout, Francesca Cella Zanacchi, Michael Mlodzianoski, Alberto Diaspro, Joerg Bewersdorf, Samuel T Hess, and Kevin Braeckmans. Precisely and accurately localizing single emitters in fluorescence microscopy. *Nature methods*, 11(3):253–266, 2014.

[27] Ratsimandresy Holinirina Dina Miora. Image processing and imaging analysis for fluorescence microscopy. Structured masters thesis, African Institute for Mathematical Sciences, June 2016.

Stellenbosch University https://scholar.sun.ac.za

[28] Raimund J Ober, Sripad Ram, and E Sally Ward. Localization accuracy in single-molecule microscopy. *Biophysical journal*, 86(2):1185–1200, 2004.

[29] Sean Quirin, Sri Rama Prasanna Pavani, and Rafael Piestun. Optimal 3d single-molecule localization for superresolution microscopy with aberrations and engineered point spread functions. *Proceedings of the National Academy of Sciences*, 109(3):675–679, 2012.

[30] Alex von Diezmann, Yoav Shechtman, and WE Moerner. Three-dimensional localization of single molecules for super-resolution imaging and single-particle tracking. *Chemical Reviews*, 2017.

[31] Ginni Grover, Sean Quirin, Callie Fiedler, and Rafael Piestun. Photon efficient double-helix psf microscopy with application to 3d photo-activation localization imaging. *Biomedical optics express*, 2(11):3010–3020, 2011.

[32] Majid Badieirostami, Matthew D Lew, Michael A Thompson, and WE Moerner. Three-dimensional localization precision of the double-helix point spread function versus astigmatism and biplane. *Applied physics letters*, 97(16):161103, 2010.

[33] Johann Engelhardt, Jan Keller, Patrick Hoyer, Matthias Reuss, Thorsten Staudt, and Stefan W Hell. Molecular orientation affects localization accuracy in superresolution far-field fluorescence microscopy. *Nano letters*, 11(1):209–213, 2010.